Green Energy and Intelligent Transportation 5 (2026) 100427

Contents lists available at ScienceDirect

Green Energy and Intelligent Transportation

journal homepage: www.journals.elsevier.com/green-energy-and-intelligent-transportation

Full length article

Global coordinated control framework for advanced all-wheel steering and driving vehicles: Unleashing potential through tire slip state assessment

Xiaoxuan Yin[a], Lei Zhang[a,b,*], Xiaolin Ding[a], Fengchun Sun[a], David Dorrell[c]

[a] *National Engineering Research Center for Electric Vehicles, Beijing Institute of Technology, Beijing 100081, China*
[b] *Advanced Technology Research Institute, Beijing Institute of Technology, Beijing 100081, China*
[c] *Department of Mechanical and Materials Engineering, University of Turku, Turku 20500, Finland*

HIGHLIGHTS

- All-wheel steering enables more diverse driving modes.
- Rational steering intention interpretation reduces driving workload.
- Considering driver input dynamics improves vehicle response.
- Tire slip state analysis enhances multi-actuator coordination efficiency.
- Efficient actuator coordination extends vehicle stability boundaries.

GRAPHICAL ABSTRACT

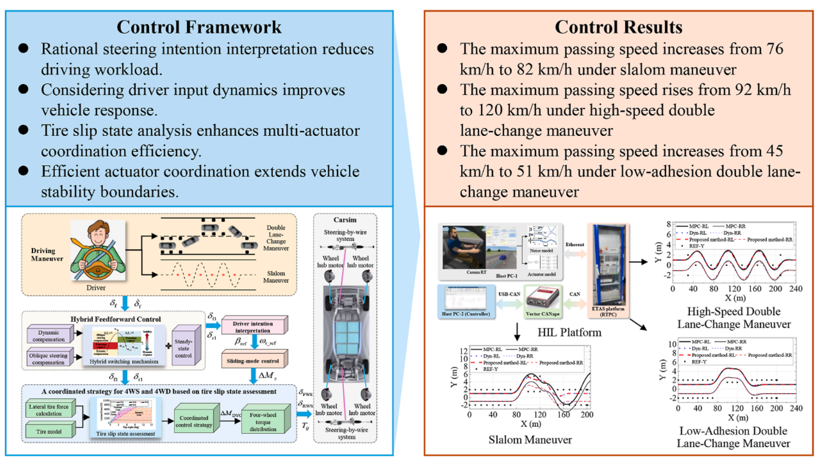

ARTICLE INFO

Keywords:
Four-wheel-steering and four-wheel-driving vehicles
Driver intention interpretation
Chassis coordinated control
Tire slip state assessment

ABSTRACT

To address the challenge of efficient actuator coordination in all-wheel steering and driving vehicles, this paper proposes a global coordinated control framework based on tire slip state assessment. First, a hybrid feedforward control method comprising steady-state control, dynamic compensation, and oblique steering compensation is proposed to respond rapidly to the driver's demands under various driving conditions. Then, considering different steering modes of four-wheel steering vehicles, a driver intention interpretation method that integrates conventional steering and oblique steering is developed. Subsequently, a sliding mode control algorithm is utilized to track the driver's desired motion states, improving the vehicle's robustness against system disturbances. Moreover, taking lateral acceleration and yaw rate as inputs, a coordinated strategy for the four-wheel steering angles and driving torques is established based on tire slip state assessment. Finally, hardware-in-the-loop test results show that, compared to the model predictive control (MPC) algorithm, the proposed control

* Corresponding author.
E-mail address: lei_zhang@bit.edu.cn (L. Zhang).

https://doi.org/10.1016/j.geits.2026.100427
Received 15 January 2026; Received in revised form 7 May 2026; Accepted 8 May 2026
Available online 15 May 2026

scheme increases the maximum speed in double lane-change maneuvers by 13%, significantly improving the vehicle handling performance under different driving conditions.

1. Introduction

Automobile electrification has emerged as a globally recognized solution to mitigate global warming effects [1–4]. Electric vehicles equipped with four-wheel steering and four-wheel driving (4WS-4WD) systems can significantly enhance safety, stability, and maneuverability through the coordinated control of the driving torques and steering angles of all wheels. However, 4WS-4WD electric vehicles also bring formidible challenges. First, 4WS-4WD electric vehicles offer a variety of steering modes, including conventional, oblique, and zero-radius steering. To accommodate diverse driver needs, it is essential to establish an effective driver intention interpretation method that offers a comprehensive understanding of the relationship between steering input and vehicle motion. On this basis, how to further coordinate 4WS and 4WD systems to enhance the overall vehicle performance is also a research focus. It has garnered significant attention from both academia and industrial practitioners.

Existing research on driver intention interpretation for 4WS-4WD electric vehicles falls into two categories. The first category ensures consistency with front-wheel steering (FWS) vehicles by interpreting driver intentions based on FWS models [5,6]. For example, Liang [6] et al. derived desired motion states from an FWS model, using rear-wheel steering (RWS) and four-wheel steering to enhance stability. However, the approach overlooks lateral force response benefits brought by RWS [7]. The second approach sets vehicle sideslip angle to zero and derives desired yaw rates and feedforward wheel angles to exploit the maneuverability and stability of 4WS vehicles [8]. On this regard, Zhang [9] et al. calculated the desired yaw rate using a bicycle model, while Loyola [10] et al. proposed a variable wheelbase reference model to improve tracking accuracy. However, these studies only focus on conventional steering modes but neglect special modes such as oblique and zero-radius steering. Additionally, the existing mode-switching mechanisms are only limited to stationary or straight-line driving conditions [11], and fail to fully exploit 4WS vehicle performance during emergency maneuvers.

For efficient 4WS-4WD coordination, two primary challenges still exist: (1) the coupling effect between the longitudinal and lateral tire forces subject to the tire adhesion ellipse, and (2) the conflicting control objectives between the four-wheel steering and four-wheel driving systems. Current chassis coordinated control methods can be broadly categorized into integrated control [12–15] and hierarchical coordinated control [16–18]. The integrated control method incorporates all control variables into a single model and achieves actuator coordination by optimizing objective weights. For instance, Liu [19] et al. proposed a nonlinear model predictive control (NMPC)-based controller to optimize vehicle yaw moment and lateral force distribution. However, it involves solving high-dimensional equations, resulting in high computational burden. Additionally, the reliance on inverse tire models for steering angle derivation makes it susceptible to signal noises.

In contrast, hierarchical coordinated control strategies allocate optimal weighting coefficients to individual actuators to achieve efficient coordination. Two predominant approaches are phase-plane-based [20–23] and tire-force-based methods [24–26]. Phase-plane-based methods analyze vehicle dynamics using $\beta\_\dot{\beta}$ [20] or β_ω_r [27,28] phase trajectories under varying initial conditions to define vehicle stability states and guide actuator weight distribution. For example, Wang [23] et al. used support vector machines to partition the $\beta\_\dot{\beta}$ phase plane into classical, extended, and unstable regions, applying active front steering (AFS) and direct yaw-moment control (DYC) accordingly. However, such methods often require extensive calibration, thus limiting their practicality. Conversely, tire-force-based methods estimate longitudinal and lateral tire forces to determine vehicle stability states and design control schemes. For example, Ding [29] et al. categorized tire forces into linear, transition, and saturation zones, applying AFS and DYC accordingly. Nevertheless, these approaches do not fully exploit the potential of integrated 4WS-4WD systems under extreme driving conditions.

To address the limitations of existing approaches, this study proposes a global coordinated control framework based on tire slip state assessment. First, a hybrid feedforward control strategy is developed, integrating steady-state control, dynamic compensation, and oblique steering compensation. Second, a driver intention interpretation strategy for conventional and oblique steering modes is established using a kinematic model. Third, a sliding mode control (SMC) algorithm is designed to compute the required corrective yaw moment. Fourth, a weight distribution mechanism for the front- and rear-wheel steering angles and individual wheel driving torques is formulated based on vehicle state information, such as lateral acceleration and yaw rate. A torque optimization method for the four-wheel drive system is proposed to minimize both the tire slip ratio and the tracking errors of the control variables. Finally, the effectiveness of the proposed scheme is validated through comprehensive Hardware-in-the-Loop tests. The main contributions of this study are summarized as follows:

- A hierarchical hybrid control architecture is proposed, integrating dynamic compensation and oblique steering compensation. Unlike conventional hierarchical structures, the framework incorporates dynamic compensation to improve transient response, while the oblique steering compensation is used to improve vehicle stability under extreme operating conditions.
- A multi-mode steering intention interpretation method is proposed. In contrast to conventional quasi-steady-state approaches, the proposed method utilizes a kinematic model to interpret desired vehicle motion for both conventional and oblique steering modes, while integrating a dynamic model to ensure stability and effectively alleviate driver workload.
- A chassis coordinated control strategy based on tire slip state assessment is introduced. Different from conventional phase-plane-based coordination methods, the proposed strategy accounts for varying control characteristics across different tire operating states, enabling efficient coordination between the steering and driving systems.

The remainder of this paper is organized as follows: Section 2 introduces the vehicle modeling. Section 3 elaborates on the proposed coordinated control architecture based on tire slip state assessment. Section 4 presents the HIL verification results, and key conclusions are summarized in Section 5.

2. Vehicle model

2.1. 2-DOF vehicle model

As shown in Fig. 1, a 2-DOF vehicle model is used to describe vehicle lateral and yaw motions, which is given by

$$\begin{aligned}
\dot{\beta} &= \frac{k_f + k_r}{m v_x}\beta + \left(\frac{a k_f - b k_r}{m v_x^2} - 1\right)\omega_r - \frac{k_f}{m v_x}\delta_f - \frac{k_r}{m v_x}\delta_r \\
\dot{\omega}_r &= \frac{a k_f - b k_r}{I_z}\beta + \frac{a^2 k_f + b^2 k_r}{I_z v_x}\omega_r - \frac{a k_f}{I_z}\delta_f + \frac{b k_r}{I_z}\delta_r
\end{aligned} \tag{1}$$

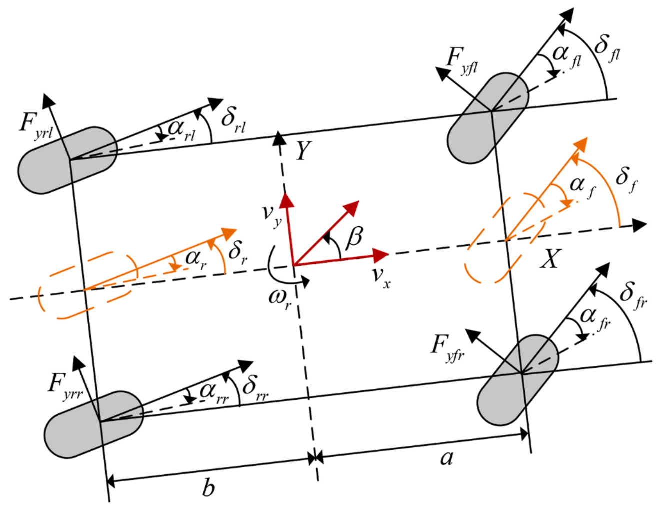

Fig. 1. The 2-DOF vehicle model.

where k_f and k_r are the ideal cornering stiffnesses of the front and rear axles; a and b are the horizontal distances from the front and rear axles to the vehicle's center of gravity (CoG); m is the vehicle mass; v_x is the vehicle longitudinal velocity; β is the vehicle sideslip angle; ω_r is the vehicle yaw rate; I_z is the moment of inertia along the z-axis; δ_f and δ_r are the steering angles of the front and rear wheels. It can be reformulated as

$$\dot{\boldsymbol{x}} = \boldsymbol{A}_0\boldsymbol{x} + \boldsymbol{B}_0\boldsymbol{\delta}_t \tag{2}$$

where $\boldsymbol{A}_0 = \begin{bmatrix} \dfrac{k_f + k_r}{mv_x} & \dfrac{ak_f - bk_r}{mv_x^2} - 1 \\ \dfrac{ak_f - bk_r}{I_z} & \dfrac{a^2k_f + b^2k_r}{I_z v_x} \end{bmatrix}$; $\boldsymbol{B}_0 = \begin{bmatrix} -\dfrac{k_f}{mv_x} & -\dfrac{k_r}{mv_x} \\ -\dfrac{ak_f}{I_z} & \dfrac{bk_r}{I_z} \end{bmatrix}$; $\boldsymbol{x} = \begin{bmatrix} \beta \\ \omega_r \end{bmatrix}$; $\boldsymbol{\delta}_t = \begin{bmatrix} \delta_{tf} \\ \delta_{tr} \end{bmatrix}$ is the actual steering angle.

2.2. Vehicle kinematics model

Traditional driver intention interpretation primarily relies on vehicle dynamics models to infer driver intentions, without analyzing vehicle motion from the driver's perspective. This approach often results in discrepancies between the driver's intentions and the vehicle's optimal motion state. To address this issue, this study employs a kinematic model to interpret driver intentions by analyzing the mapping relationship between the steering angles of the front and rear wheels and the vehicle's cornering radius. As shown in Fig. 2, for the triangles OCA and OCB, we have [30]

$$\frac{\sin(\delta_f - \beta)}{a} = \frac{\sin(\pi/2 - \delta_f)}{R} \tag{3}$$

$$\frac{\sin(\beta - \delta_r)}{b} = \frac{\sin(\pi/2 + \delta_r)}{R} \tag{4}$$

where R is the vehicle's cornering radius.

Simplify Eqs. (3) and (4) and we get

$$(\tan\delta_f - \tan\delta_r)\cos\beta = (a+b)/R \tag{5}$$

The cornering radius is given by

$$R = \frac{(a+b)}{(\tan\delta_f - \tan\delta_r)\cos\beta} \tag{6}$$

Furthermore, the driver's desired yaw rate is obtained by

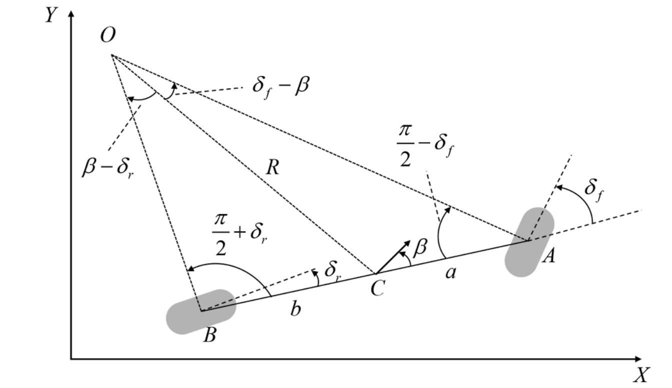

Fig. 2. The vehicle kinematics model.

$$\omega_{rd} = \frac{v_x}{R} = \frac{v_x(\tan\delta_f - \tan\delta_r)\cos(\beta)}{a+b} \tag{7}$$

The front-wheel steering angle is determined by

$$\delta_f = \delta_{sw}/i_w \tag{8}$$

where δ_{sw} is the wheel steering angle; i_w is the steering ratio from the steering wheel to the front wheels. The variable steering ratio is given by [9]

$$i_w = \begin{cases} 8.5 & v_x \in [0, 40\ \text{km/h}]\&i_{wr} < 8.5\text{s}^{-1} \\ i_{wr} & v_x \in [0, 40\ \text{km/h}]\&i_{wr} \geq 8.5\text{s}^{-1} \\ \chi i_{wr} + (1-\chi)i_{\text{fixed}} & v_x \in [40\ \text{km/h}, 90\ \text{km/h}] \\ 21.5 & v_x \in [90\ \text{km/h}, 150\ \text{km/h}] \end{cases} \tag{9}$$

$$i_{wr} = \frac{v_x/G_{wr}}{1 + mbv_x^2/(2(a+b)ak_f)} \tag{10}$$

$$\chi = (i_{\max} - i_{\min}) \Big/ \left(1 + \exp\left(-\frac{v_x - (v_2 + v_1)/2}{1.3}\right)\right) + i_{\min} \tag{11}$$

where i_{fixed} is the fixed steering ratio set to be 21.5; i_{wr} is a fixed yaw rate gain-based variable steering ratio; χ is the steering ratio weighting coefficient; $i_{\min}$ and $i_{\max}$ are the maximum and minimum steering ratios in the transition zone that are set to be 18.55 and 21.5; G_{wr} is the yaw rate gain set to be 0.24 s^{-1}; v_1 and v_2 are the vehicle longitudinal velocities corresponding to the endpoints of the transition zone [40 km/h, 90 km/h].

3. The proposed coordinated control architecture based on tire slip state assessment

To improve the extreme obstacle avoidance capability of four-wheel steering and four-wheel drive vehicles while reducing the driver's workload, this study proposes a combined feedforward and feedback control framework to coordinate four-wheel steering angles and driving torques. First, a hybrid feedforward control method is developed, integrating the steady-state control, dynamic compensation, and oblique steering compensation to address varying control requirements under different operating conditions. Then a kinematic model-based driver intention interpretation method is established to provide the desired motion state. Furthermore, a sliding mode control algorithm is employed to track the desired vehicle motion state. Finally, a coordinated control strategy is designed based on lateral acceleration and yaw rate signals. The schematic of the proposed control scheme is illustrated in Fig. 3.

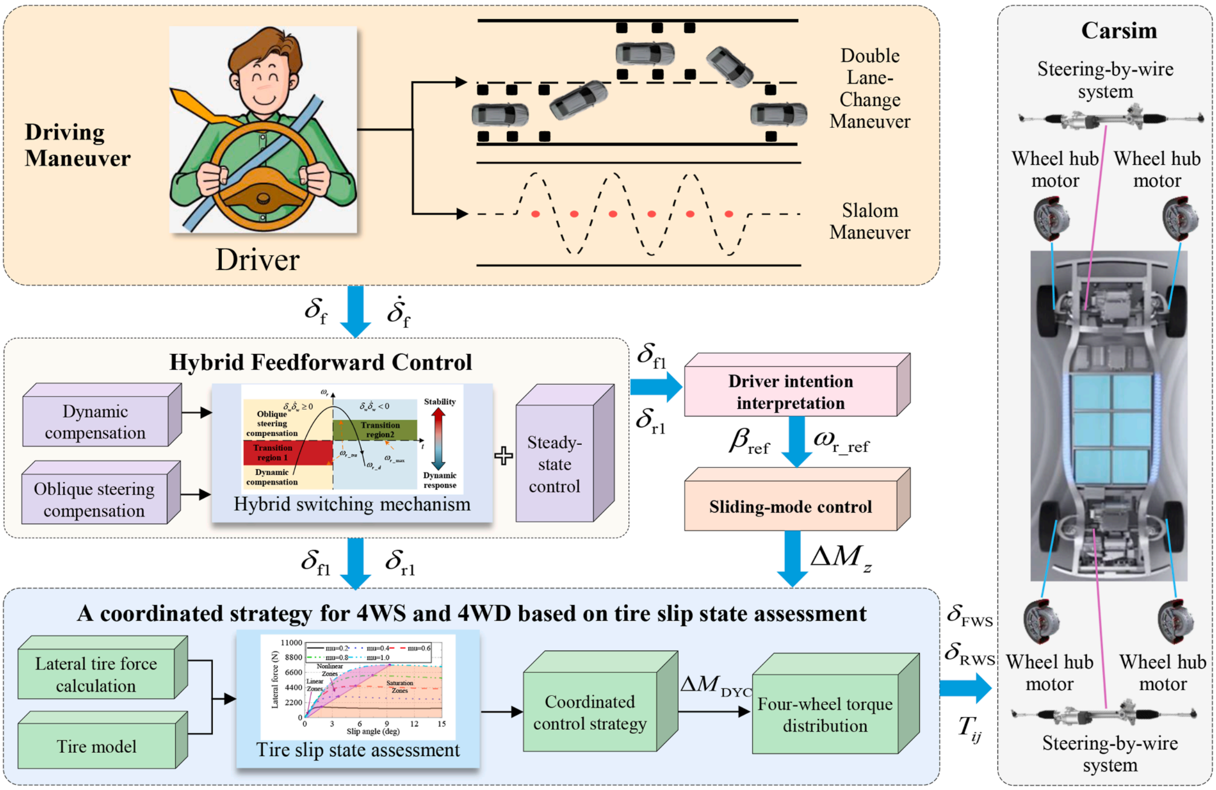

Fig. 3. The schematic of the proposed coordinated control framework.

3.1. *Hybrid feedforward controller design*

Considering the constraints of the maximum yaw rate and road adhesion, a hybrid feedforward control scheme is developed by integrating the steady-state control, dynamic compensation, and oblique steering compensation.

3.1.1. *Steady-state control*

Steady-state control refers to the steady-state dynamics equation of the 2-DOF vehicle, which is given by

$$\mathbf{0} = \boldsymbol{A}_0\boldsymbol{x} + \boldsymbol{B}_0\boldsymbol{u}_s \tag{12}$$

where $\boldsymbol{u}_s = \left[\delta_{f\_s},\ \delta_{r\_s}\right]^T$ is the steering angle of the front and rear wheels under steady-state conditions, which can be calculated by

$$\begin{aligned}&\delta_{f\_s} = \delta_f\\ &\delta_{r\_s} = -\frac{(a+b)bk_fk_r + ak_fmv_x^2}{a(a+b)k_fk_r - bk_rmv_x^2}\delta_f\end{aligned} \tag{13}$$

3.1.2. *Dynamic compensation control*

During vehicular operation, the driver's desired state varies continuously with time. The yaw rate obtained from the steady-state theory is insufficient to fully capture the driver's dynamic maneuvers. To address this limitation, a dynamic compensation mechanism is introduced to enhance time-varying reference state tracking accuracy. It should be noted that the following assumptions are made: 1) To ensure that the vehicle's velocity direction remains aligned with its heading and to maximize the utilization of available tire forces, the desired sideslip angle is set to zero, which means $\beta = 0$ and $\dot\beta = 0$; 2) As this study focuses on extreme operating conditions involving large steering angles, the variation in the longitudinal velocity is much slower than the lateral dynamics. Therefore, the longitudinal vehicle velocity is assumed to remain constant.

Taking the front-wheel steering angle rate as the input, the change of the desired motion states can be expressed as

$$\begin{aligned}&\dot\beta = 0\\ &\dot\omega_{rd} = \frac{v_x}{\dot R} = \frac{v_x\left(\dot\delta_f/\left(\cos^2\delta_f\right) - \dot\delta_r/\left(\cos^2\delta_r\right)\right)}{a+b}\end{aligned} \tag{14}$$

$$\dot\delta_r = -\frac{(a+b)bk_fk_r + ak_fmv_x^2}{a(a+b)k_fk_r - bk_rmv_x^2}\dot\delta_f \tag{15}$$

Introduce the dynamic compensation control entity $\boldsymbol{u}_{dc} = \left[\delta_{f\_dc}, \delta_{r\_dc}\right]^T$ such that it satisfies

$$\dot{\boldsymbol{x}} = \boldsymbol{A}_0\boldsymbol{x} + \boldsymbol{B}_0(\boldsymbol{u}_s + \boldsymbol{u}_{dc}) \tag{16}$$

Based on the desired change rate of yaw rate, the dynamic compensation for the vehicle is derived by

$$\begin{aligned}&\delta_{f\_dc} = \frac{I_z}{(a+b)k_f}\dot\omega_{rd}\\ &\delta_{r\_dc} = -\frac{I_z}{(a+b)k_r}\dot\omega_{rd}\end{aligned} \tag{17}$$

3.1.3. *Oblique steering compensation*

Considering the road adhesion limit, the maximum ideal yaw rate is expressed as [31]

$$\omega_{r\_max} = 0.85\mu g^*\mathrm{sgn}\left(\delta_f\right)/v_x \tag{18}$$

where g is the acceleration of gravity.

The maximum front-wheel steering angle permitted by the road surface adhesion is

$$\delta_{\mathrm{f\_max}} = \frac{a(a+b)k_{\mathrm{f}}k_{\mathrm{r}} - bk_{\mathrm{r}}mv_x^2}{(a^2-b^2)k_{\mathrm{f}}k_{\mathrm{r}} - (ak_{\mathrm{f}} + bk_{\mathrm{r}})mv_x^2}\frac{(a+b)}{v_x}\omega_{\mathrm{r\_max}} \tag{19}$$

When the front-wheel steering angle exceeds the maximum limit imposed by road adhesion, an oblique steering compensation strategy is employed. The compensation steering angles for the front and rear wheels are given by

$$\delta_{\mathrm{f\_oc}} = \delta_{\mathrm{r\_oc}} = \delta_{\mathrm{f}} - \delta_{\mathrm{f\_max}} \tag{20}$$

3.1.4. Hybrid feedforward control

In the feedforward control, the steady-state control module primarily responds to the driver's inputs. In contrast, the dynamic compensation control module addresses the dynamic variations in the vehicle's desired motion state and is primarily active within the vehicle's stability region. Additionally, the oblique steering compensation control module is designed to enhance vehicle stability and activates when the vehicle's motion state exceeds the road adhesion limit. To optimize the performance of each feedforward control module, this study proposes a hybrid feedforward control strategy. The core principle involves designing weighting coefficients for the dynamic compensation and oblique steering compensation based on the desired yaw rate, and subsequently generating the feedforward wheel angles using these weighting coefficients.

When the steering wheel angle exceeds the maximum limit permitted by road adhesion, the vehicle's yaw motion approaches the stability boundaries. At this stage, the control objective transitions from dynamic response regulation to stability maintenance. Consequently, the control system switches from the dynamic compensation module to the oblique steering compensation module. To ensure a smooth transition between the compensation modes, a smooth switching function is designed as

$$\eta_1 = \frac{1 - \tanh(\mathrm{abs}(\omega_{\mathrm{rd}} - \omega_{\mathrm{r\_tran}})/(\omega_{\mathrm{r\_tran}})\rho_1)}{2} \tag{21}$$

where tanh(.) is the hyperbolic tangent function; $\omega_{\mathrm{r\_tran}}$ is the control boundary of the yaw rate; ρ_1 is the correction factor for adjusting the control weights.

Under the oblique steering compensation module, the yaw rate decreases rapidly, resulting in compromised steering performance. This prompts the driver to apply a larger steering wheel angle, thereby increasing the driver's burden. To maintain superior steering performance, the oblique steering compensation module should not remain engaged for an extended period. This study utilizes the yaw rate information to limit the oblique steering compensation control duration. In particular, the module is deactivated when the vehicle's actual yaw rate falls below 90% of its maximum value. To prevent abrupt changes in the wheel steering angles, a hyperbolic tangent function is employed to ensure a smooth exit process, which is given by

$$\eta_2 = \begin{cases} 0.5 - 0.5\tanh\left(\dfrac{|0.9\omega_{\mathrm{r\_tran}} - \omega_{\mathrm{r}}|}{\omega_{\mathrm{r\_tran}}\rho_2}\right) & \text{if } \omega_{\mathrm{rd}} > \omega_{\mathrm{r\_tran}}, \\ 0 & \text{if } \omega_{\mathrm{rd}} \le \omega_{\mathrm{r\_tran}}. \end{cases} \tag{22}$$

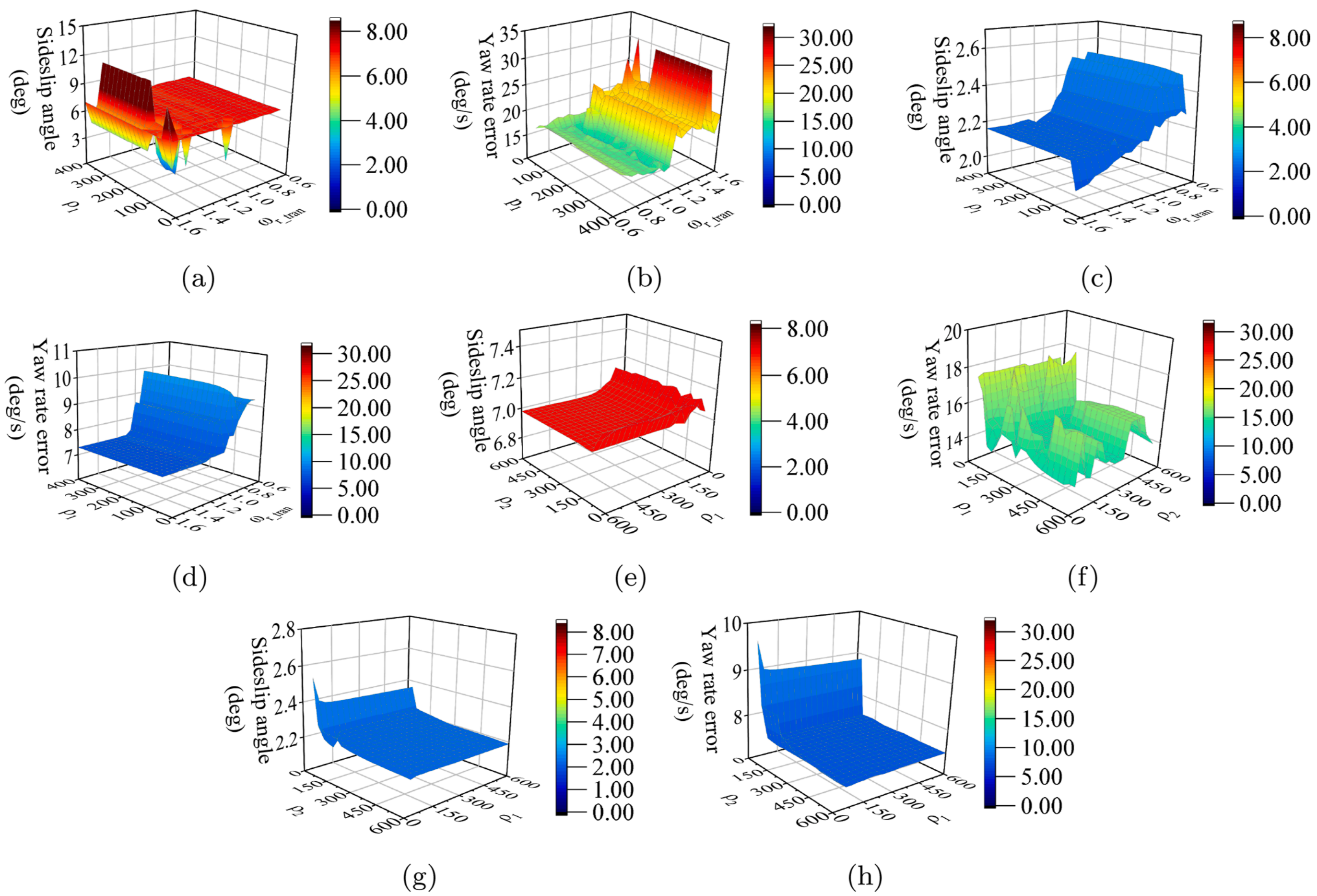

Fig. 4. The graph of vehicle performance variation with feedforward control parameters changes. (a) sideslip angle with $\omega_{\mathrm{r\_tran}}$ and ρ_1 (μ=0.35); (b) yaw rate error with $\omega_{\mathrm{r\_tran}}$ and ρ_1 (μ=0.35); (c) sideslip angle with $\omega_{\mathrm{r\_tran}}$ and ρ_1 (μ=0.85); (d)yaw rate error with $\omega_{\mathrm{r\_tran}}$ and ρ_1 (μ=0.85); (e) sideslip angle with ρ_1 and ρ_2 (μ=0.35); (f)yaw rate error with ρ_1 and ρ_2 (μ=0.35); (g) sideslip angle with ρ_1 and ρ_2 (μ=0.85); (h)yaw rate error with ρ_1 and ρ_2 (μ=0.85).

where ρ_2 is the smooth weight coefficient for the exit process of the oblique condition, which is set to 100. In summary, the feedforward front and rear wheel steering angles are derived as

$$\begin{aligned} \delta_{f1} &= \eta_1\delta_{f\_dc} + \eta_2\delta_{f\_oc} + \delta_{f\_s} \\ \delta_{r1} &= \eta_1\delta_{r\_dc} + \eta_2\delta_{r\_oc} + \delta_{r\_s} \end{aligned} \tag{23}$$

According to Equations (21) and (22), the parameter ω_{r_tran} determines the switching timing between the dynamic compensation and oblique steering compensation. ρ_1 and ρ_2 are used to regulate the switching rate of the feedforward control between these two modes. As shown in Fig.4a–b, the vehicle has a higher demand for stability due to the limited tire force margin under low-adhesion conditions. As ω_{r_tran} increases, the feedforward control switches later to the oblique steering compensation mode, leading to larger sideslip angles and greater yaw rate tracking errors. Under high-speed conditions ((Fig.4c–d)), rapid response to driver's input is more important. A smaller ω_{r_tran} keeps the controller longer in the dynamic compensation mode, thereby improving the driver's steering intention tracking accuracy. The effects of ρ_1 and ρ_2 are illustrated in Fig.4e–h. Within a reasonable range, their impact on control performance is limited. However, when either of the two parameters is too small, the control performance would be remarkably compromised. If ρ_1 is too small, the controller will be dominated by the dynamic compensation mode and cannot fully switch to the oblique steering compensation mode under extreme conditions. If ρ_2 is too small, the controller cannot exit the oblique steering compensation mode in time, resulting in degraded tracking performance. In a nutshell, although the feedforward parameters influence the high- and low-adhesion conditions differently, there exists an overlapping parameter range that ensures satisfactory control performance in both scenarios.

3.2. State error feedback controller design

To further enhance vehicle performance, eliminate tracking errors, and improve robustness against external disturbances and model parameter uncertainties, a closed-loop error feedback controller is designed based on the sliding mode control algorithm.

3.2.1. Driver intention interpretation

In the feedforward control, this study employs a hybrid feedforward control strategy that integrates the steady-state control, dynamic compensation, and oblique steering compensation to address the driver's diverse intentions. The dynamic compensation module is utilized to account for the driver intentions. Consequently, in the driver intention interpretation, this study focuses on the impacts of the conventional steering and oblique steering compensation on the ideal vehicle motion state. The desired vehicle motion state under conventional steering conditions can be determined using Equation (7). However, when the vehicle operates under the oblique steering compensation module, the desired sideslip angle deviates from zero, as the front and rear wheels are compensated for with identical steering angles. By substituting Equations (13) and (20) into the vehicle dynamics Equation (2), we derive the simplified expression as

$$\dot{\boldsymbol{x}} = \boldsymbol{A}_0\boldsymbol{x} + \boldsymbol{B}_0(\boldsymbol{u}_s + \boldsymbol{u}_{oc}) \tag{24}$$

where $\boldsymbol{u}_{oc} = [\delta_{f\_oc}, \delta_{r\_oc}]^T$.

Then the desired state under the oblique steering compensation module can be derived as

$$\begin{aligned} \beta_d &= \delta_{f\_oc} = \delta_{r\_oc} \\ \omega_{rd} &= \omega_{r\_max} \end{aligned} \tag{25}$$

Furthermore, considering the road adhesion limit, the reference vehicle state is corrected as [32]

$$\begin{aligned} \beta_{ref} &= \min(\beta_d, \arctan(0.02\mu g)) \\ \omega_{r\_ref} &= \min(\omega_{rd}, \omega_{r\_max}) \end{aligned} \tag{26}$$

The driver's desired vehicle motion state during the vehicle cornering process can be interpreted as

$$\begin{aligned} \beta_{ref} &= \begin{cases} 0 & \delta_f \le \delta_{f\_max} \\ \min(\delta_f - \delta_{f\_max}, \arctan(0.02\mu g)) & \delta_f > \delta_{f\_max} \end{cases} \\ \omega_{r\_ref} &= \begin{cases} \omega_{rd} & \delta_f \le \delta_{f\_max} \\ \omega_{r\_max} & \delta_f > \delta_{f\_max} \end{cases} \end{aligned} \tag{27}$$

3.2.2. Closed-loop system error feedback controller design

The system tracking error is defined as $\boldsymbol{e} = [\beta_e, \omega_{re}]^T = [\beta - \beta_{ref}, \omega_r - \omega_{r\_ref}]^T$. The discrete state error equation of the closed-loop system becomes

$$\boldsymbol{e}(k+1) = \overline{\boldsymbol{A}}\boldsymbol{e}(k) + \overline{\boldsymbol{B}}u_e(k) \tag{28}$$

where $\overline{\boldsymbol{A}} = \begin{bmatrix} \frac{k_f + k_r}{mv_x}T_s + 1 & \left(\frac{ak_f - bk_r}{mv_x^2} - 1\right)T_s \\ \frac{ak_f - bk_r}{I_z}T_s & \frac{a^2k_f + b^2k_r}{I_z v_x}T_s + 1 \end{bmatrix}$; $\overline{\boldsymbol{B}} = [0, T_s/I_z]^T$; $u_e = \Delta M_z$; T_s is the sampling time; ΔM_z is the total additional yaw moment; k is the kth discrete sampling point.

Sliding mode control drives the controlled system onto a predefined sliding surface and constrains its motion along it [33]. Compared with the NMPC and adaptive control approaches, SMC exhibits strong robustness to modeling uncertainties and external disturbances. Its low computational burden also satisfies the real-time requirements of chassis control. For these reasons, SMC is adopted as the feedback control method here. However, SMC has two main limitations. First, conventional SMC suppresses uncertainties and disturbances through high-frequency switching, resulting in chattering near the sliding surface. Second, the control performance largely depends on the initial state. When the initial state is far from the sliding surface, the system converges very slowly, leading to poor control performance. To address these issues, a saturation function is introduced to mitigate the chattering phenomenon. Moreover, a hybrid feedforward scheme is designed to enhance the vehicle's response to the driver's inputs, reducing the initial deviation from the sliding surface.

Based on the tracking errors of the yaw rate and sideslip angle, the sliding mode surface is designed as

$$\begin{aligned} s(k) &= c^*(\omega_{re}(k)) + d^*(\beta_e(k)) \\ s(k+1) &= c^*(\omega_{re}(k+1)) + d^*(\beta_e(k+1)) \end{aligned} \tag{29}$$

where s is the sliding surface; c is the weight for the yaw rate tracking error; d is the weight for the sideslip angle tracking error.

Substituting the state error equation into the sliding mode surface, we get

$$\begin{aligned} s(k+1) = {} & c\frac{ak_f - bk_r}{I_z}T_s\beta_e(k) \\ & + c\left(\frac{a^2k_f + b^2k_r}{I_z v_x}T_s + 1\right)\omega_{re}(k) \\ & + c\frac{T_s}{I_z}u_e(k) + d\left(\frac{k_f + k_r}{mv_x}T_s + 1\right)\beta(k) \\ & + d\left(\frac{ak_f - bk_r}{mv_x^2} - 1\right)T_s\omega_{re}(k) \end{aligned} \tag{30}$$

The approaching rate of the designed sliding mode controller is

$$s(k+1) = -\epsilon T_s sat(s(k)) + (1 - \lambda T_s)s(k) \tag{31}$$

where ϵ and λ are the parameters of the sliding mode approaching rate.

To prevent controller chattering, a saturation function is used to achieve smooth switching near the sliding mode surface, which is given by

$$sat(s(k)) = \begin{cases} 1 & s(k) > \Phi \\ s(k)/\Phi & |s(k)| \le \Phi \\ -1 & s(k) < -\Phi \end{cases} \tag{32}$$

where Φ is the transition zone of the sliding mode surface, which is set to 0.01.

The sliding mode control law is derived as

$$\begin{aligned}\Delta M_z &= -c\frac{I_z}{T_s}\frac{ak_f - bk_r}{I_z}T_s\beta_e(k) - c\frac{I_z}{T_s}\left(\frac{a^2k_f + b^2k_r}{I_z v_x}T_s + 1\right)\omega_{re} \\ &\quad -d\frac{I_z}{T_s}\left(\frac{k_f + k_r}{mv_x}T_s + 1\right)\beta_e(k) - d\frac{I_z}{T_s}\left(\frac{ak_f - bk_r}{mv_x^2} - 1\right)T_s\omega_{re} \\ &\quad -\frac{I_z}{T_s}(\epsilon T_s sat(s(k)) + (1 - \lambda T_s)s(k))\end{aligned} \tag{33}$$

3.2.3. Proof of system stability

From the feedforward control calculation Equation (23), it is evident that the driver's input determines the feedforward control. In contrast, the feedback control ensures vehicle stability by tracking the desired motion state. Consequently, the feedforward control have little influence on the overall system stability. This study focuses on proving the stability of the closed-loop error feedback system using the Lyapunov's direct method. The Lyapunov function is defined as

$$V(k) = \frac{1}{2}s^2(k) \tag{34}$$

The increment of the Lyapunov function is

$$\Delta V = V(k+1) - V(k) = \frac{1}{2}s^2(k+1) - \frac{1}{2}s^2(k) \tag{35}$$

Substituting it into ΔV gives

$$\Delta V = \frac{1}{2}[(1 - \lambda T_s)s(k) - \epsilon T_s sat(s(k))]^2 - \frac{1}{2}s(k)s(k) \tag{36}$$

$$[(1 - \lambda T_s)s(k)]^2 = (1 - \lambda T_s)^2 s(k)s(k) \tag{37}$$

$$2(1 - \lambda T_s)s(k)\epsilon T_s sat(s(k)) \le 2\epsilon T_s(1 - \lambda T_s)\|s(k)\| \tag{38}$$

where $\|s(k)\|$ is the norm of $s(k)$.

Substituting it into the system increment, we get

$$\begin{aligned}\Delta V &= \frac{1}{2}\left[(1 - \lambda T_s)^2 s(k)s(k) + \epsilon^2 T_s^2\right] - \epsilon T_s(1 - \lambda T_s)\|s(k)\| - \frac{1}{2}s(k)s(k) \\ &= \frac{1}{2}\left[\left(-2\lambda T_s + \lambda^2 T_s^2\right)s^2(k) + \epsilon^2 T_s^2\right] - \epsilon T_s(1 - \lambda T_s)\|s(k)\|\end{aligned} \tag{39}$$

In this study, the control parameters are defined as $\lambda = 10$ and $\epsilon = 0.35$. It can be calculated that when $|s(k)| > 1.8*10^{-3}$, $\Delta V < 0$, indicating that the closed-loop error system is asymptotically stable. To further determine its stability, a finite-time convergence analysis is conducted.

Expanding the sliding mode dynamic equation, we get

$$\begin{aligned}|s(k+1)| &= |(1 - \lambda T_s)s(k) - \epsilon T_s sat(s(k))| \\ &\le (1 - \lambda T_s)|s(k)| - \epsilon T_s\end{aligned} \tag{40}$$

To ensure $|s(k+1)| < |s(k)|$, it must satisfy $|s(k)| > \epsilon T_s/(\lambda T_s) = \epsilon/\lambda$. Therefore, when $|s(k)| > \epsilon/\lambda = 0.035$, the sliding mode variable $s(k)$ gradually decreases and eventually enters the boundary layer. When $|s(k)| \le \epsilon/\lambda = 0.035$, the dynamic equation approaches $|s(k+1)| = |-\epsilon T_s sat(s(k))|$, and $s(k)$ converges to zero.

The closed-loop system can reach the boundary layer in finite time and ultimately converge to zero. Therefore, the closed-loop error feedback system is asymptotically stable.

3.3. The proposed coordinated strategy for four-wheel steering and four-wheel driving based on tire slip state assessment

The FWS, RWS, and 4WD actuation systems can independently track the driver's desired motion state. However, the control effectiveness of each actuation system varies depending on vehicle state. To fully exploit the control performance of each actuation system and to enhance the vehicle stability under extreme conditions, a coordination scheme for four-wheel steering angles and four-wheel driving torques is developed based on tire slip state assessment. The total required additional yaw moment is generated by coordinating the three actuation systems. The total additional yaw moment is given by

$$\Delta M_z = \begin{cases} -ak_f\delta_{FWS} & \text{FWS controller} \\ bk_r\delta_{RWS} & \text{RWS controller} \\ \Delta M_{4WD} & \text{4WD controller} \end{cases} \tag{41}$$

where δ_{FWS} is the front-wheel steering angles; δ_{RWS} is the rear-wheel steering angle; ΔM_{4WD} is the additional yaw moment generated by the four-wheel driving torques.

3.3.1. Lateral tire force calculation

During vehicle motion, the movement can be decomposed into two components: the circular motion around the steering center and the rotational motion around CoG. Thus, the lateral acceleration of a single axle is given by [29]

$$\begin{aligned}a_{yf} &= a_y + a\dot{\omega}_r \\ a_{yr} &= a_y - b\dot{\omega}_r\end{aligned} \tag{42}$$

where a_{yf} and a_{yr} are the steering angles of the front and rear axles; a_y is the vehicle lateral acceleration.

Considering the effects of longitudinal and lateral accelerations, the vertical loads at the four wheels are calculated by

$$\begin{aligned}F_{zfl} &= \frac{m}{(a+b)}\left(0.5gb - 0.5a_x h_g - \frac{b}{l_w}a_y h_g\right) \\ F_{zfr} &= \frac{m}{(a+b)}\left(0.5gb - 0.5a_x h_g + \frac{b}{l_w}a_y h_g\right) \\ F_{zrl} &= \frac{m}{(a+b)}\left(0.5ga + 0.5a_x h_g - \frac{a}{l_w}a_y h_g\right) \\ F_{zrr} &= \frac{m}{(a+b)}\left(0.5ga + 0.5a_x h_g + \frac{a}{l_w}a_y h_g\right)\end{aligned} \tag{43}$$

where a_x is the vehicle longitudinal acceleration; h_g is the height of CoG; l_w is the track width.

Based on the vertical loads of the four wheels, the equivalent load mass for each wheel is obtained as [34]

$$\begin{aligned}m_{fl} &= F_{zfl}/g \\ m_{fr} &= F_{zfr}/g \\ m_{rl} &= F_{zrl}/g \\ m_{rr} &= F_{zrr}/g\end{aligned} \tag{44}$$

where f and r are the front and rear axles; l and r are the wheels on the left and right sides.

Therefore, the lateral force of each wheel can be obtained as

$$\begin{aligned}F_{yfl} &= m_{fl}a_{yf} \\ F_{yfr} &= m_{fr}a_{yf} \\ F_{yrl} &= m_{rl}a_{yr} \\ F_{yrr} &= m_{rr}a_{yr}\end{aligned} \tag{45}$$

To validate the effectiveness of the proposed tire lateral force calculation method, two test scenarios were set up, including the steering angle step input and the double lane change maneuver. In these test scenarios, the Magic Formula tire model and the actual tire forces from CarSim (used as the actual tire forces) are compared. In the steering angle step input maneuver, the steering angle is set to 3°. The vehicle speed is 90 km/h, and the road adhesion coefficient is 0.85. For the double lane change maneuver, the vehicle speed is 90 km/h and the road adhesion coefficient is 0.85.

The simulation results in Fig. 5a indicate that when the steering angle is zero, a certain deviation exists between the lateral force obtained under the proposed method and the actual tire force from CarSim. This is because the proposed acceleration-based lateral force calculation method cannot capture the tire forces generated by the vehicle's structural characteristics, originating from the kingpin inclination and camber angle. During the steering process, the proposed acceleration-based lateral force calculation method exhibits a delay compared to that obtained from the Magic Formula model, while its delay relative to the actual tire force from CarSim is relatively small and can be neglected. This can be ascribed to that the acceleration-based method calculates the tire forces from the vehicle dynamic response, which inherently accounts for the dynamic lags of the tire and vehicle systems. In contrast, the Magic Formula model is a purely static model that excludes the dynamic buildup process of the tire lateral force. As shown in Fig. 5b, when the vehicle operates under extreme conditions, the lateral force calculated from the Magic Formula model exhibits significant deviation from the actual tire lateral force. In contrast, the proposed acceleration-based method can accurately capture the tire lateral force.

In a nutshell, the Magic Formula model provides a fast response in estimating tire lateral force, but its accuracy is limited under extreme conditions. The proposed acceleration-based lateral force calculation method can accurately describe the actual force state of the vehicle with higher accuracy and shows better consistency and engineering applicability under extreme conditions.

3.3.2. Interval division of the tire slip characteristics

To evaluate the slip state of each tire, the Magic Formula model is introduced as [35]

$$F_{y0}(\alpha) = \frac{\tan\alpha}{\sqrt{s_{\text{tire}}^2 + (\tan\alpha)^2}} D_y \sin\left[C_y \arctan\left(B_y\alpha - E_y\left(B_y\alpha - \arctan\left(B_y\alpha\right)\right)\right)\right] \tag{46}$$

where s_{tire} is the tire slip ratio; α is the tire slip angle; B_y, C_y and E_y are less affected by the vertical load and road adhesion coefficient, which is set as $B_y = 7.098$, $C_y = 2.216$, and $E_y = 1.009$. The tire peak adhesion coefficient D_y is significantly affected by the vertical load, which is given by

$$D_y = a_0 F_{\text{zij}}^2 + a_1 F_{\text{zij}} \tag{47}$$

where a_0 and a_1 are the fitting parameters of the vertical load, obtained by fitting the tire lateral force data under different vertical loads, and the basic road adhesion coefficients are $a_0 = -9.742$ and $a_1 = 1056$.

Considering the influence of the road adhesion coefficient, the tire force under different adhesion coefficients is given by

$$F_y = \mu F_{y0}(\alpha/\mu) \tag{48}$$

Tire force characteristics under varying road adhesion coefficients are obtained from the tire testing data generated in CarSim. As shown in Fig. 6, at small slip angles, the lateral force exhibits a linear relationship with the slip angle, indicating that the tire can generate sufficient lateral force to meet the driver intentions. As the slip angle increases, this relationship becomes nonlinear until the tire reaches saturation. Beyond this point, the lateral force alone is insufficient to accurately track the desired vehicle motion. To address this limitation, the tire slip state is divided into three distinct zones: linear, nonlinear, and saturation.

To accurately delineate the linear and nonlinear regions of tire, this study introduces the concept of a tire linear zone threshold, defined as the ratio of the slope at the boundary point between the linear and nonlinear zones to the slope at the origin of the tire slip curve. Based on this definition, the sensitivity of vehicle dynamic responses to variations is analyzed across different vehicle speeds and road adhesion coefficients. The corresponding simulation results are presented in Fig. 7.

As shown in Fig. 7a and b, when vehicle speed exceeds 45 km/h under low-adhesion conditions, the influence of the tire linear zone threshold on vehicle dynamics increases sharply. If the threshold is set too low, control is dominated by the steering system. Under such conditions, the steering-controlled tires are prone to saturation, hindering the fulfillment of control objectives. Conversely, if the threshold is set too high, control relies primarily on the driving torque. This reliance increases the likelihood of tire slip, thereby degrading vehicle stability. These findings underscore the necessity of coordinating steering angles and driving torques to fully exploit the available tire forces.

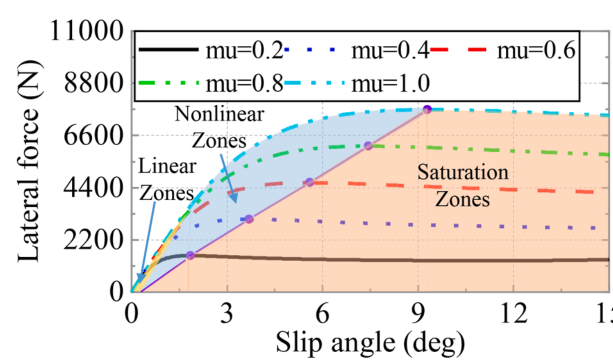

Fig. 6. The graph of tire slip characteristics varying with the road adhesion coefficient.

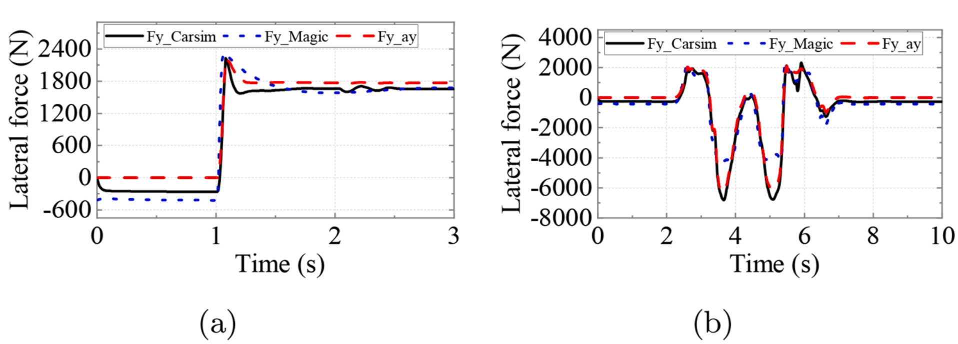

Fig. 5. The results of tire force calculation using different methods: (a) steering angle step input maneuver; (b) double lane change maneuver.

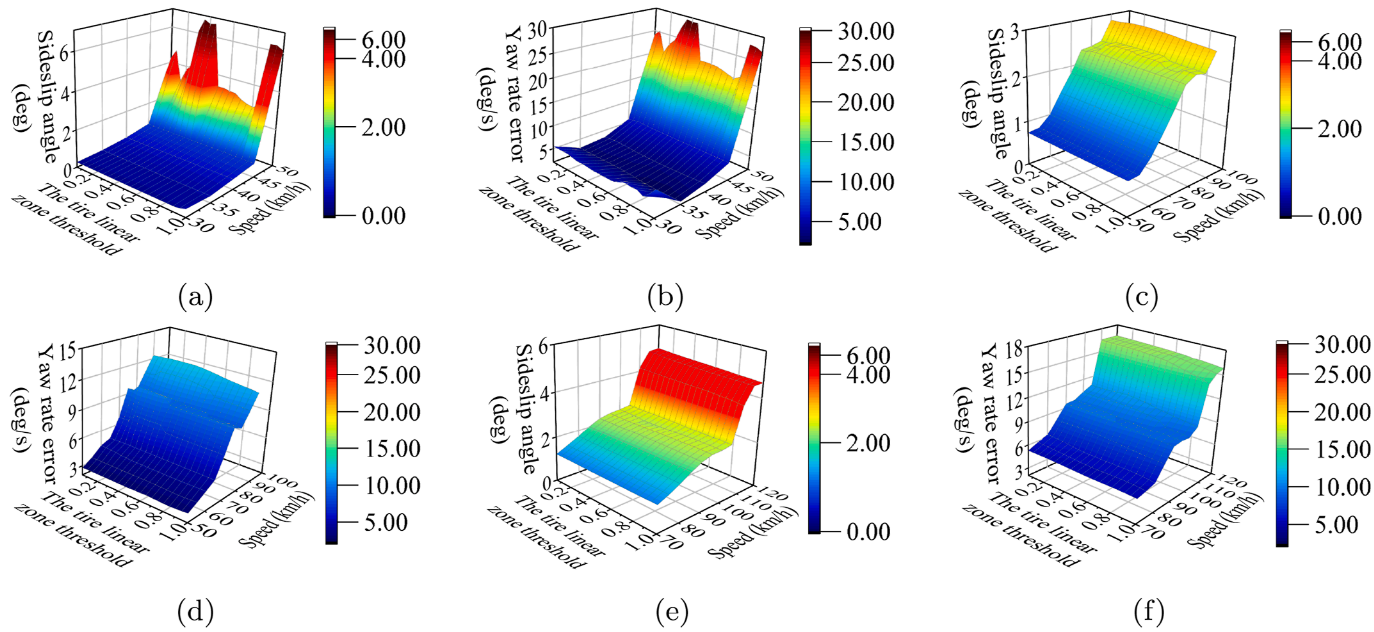

Fig. 7. The graph of vehicle performance variation with the tire linear zone threshold: (a) sideslip angle (μ=0.35); (b) yaw rate error (μ=0.35); (c) sideslip angle (μ=0.6); (d)yaw rate error (μ=0.6); (e) sideslip angle(μ=0.85); (f) yaw rate error (μ=0.85).

The results presented in Fig. 7c–f indicate that, under medium- and high-adhesion conditions, the sensitivity of vehicle dynamics to the tire linear zone threshold diminishes as the available tire force increases. For a road adhesion coefficient of 0.6, the threshold influences vehicle behavior only when the vehicle speed exceeds 80 km/h. In contrast, on a high-adhesion road (μ), vehicle dynamics exhibit limited sensitivity to the threshold and are predominantly governed by vehicle speed.

The results presented in Fig. 7c–f indicate that, under medium- and high-adhesion conditions, the sensitivity of vehicle dynamics to the tire linear zone threshold diminishes as the available tire force increases. For a road adhesion coefficient of 0.6, the threshold influences vehicle behavior only when the speed exceeds 80 km/h. In contrast, on a high-adhesion road (μ), vehicle dynamics exhibit limited sensitivity to the threshold and are predominantly governed by vehicle speed. Overall, the simulation results reveal a clear trend: as vehicle speed increases and road adhesion decreases, vehicle dynamics become more sensitive to the selection of the tire linear zone threshold. Based on the comprehensive analysis across various road adhesion levels and vehicle speeds, this study adopts a threshold value of 0.8, corresponding to a reduction of 20% in cornering stiffness relative to the strict linear region. Specifically, for a tire model with μ=1.0, the tire is assumed to work in the strict linear zone when the slip angle is below 1°. If the slope of the lateral force versus slip angle decreases by less than 20% compared with that in the strict linear zone, the tire remains in the linear zone. Once the slope reduction exceeds 20%, the tire transitions to the nonlinear zone. Finally, when the slip angle surpasses the value associated with the peak lateral force, the tire enters the saturation zone. The boundaries between these zones are primarily dictated by the road adhesion coefficient, and the specific slip angles defining these transitions are summarized in Table .1.

Table 1
The intersection points of slip characteristic intervals.

Road adhesion coefficient	0.2	0.4	0.6	0.8	1.0
Intersection of linear and nonlinear zones α_1	0.45	0.80	1.15	1.50	1.90
Intersection of nonlinear and saturation zones α_2	1.85	3.70	5.60	7.45	9.30

3.3.3. The coordinated control strategy

A coordinated control strategy for four-wheel steering and four-wheel drive is developed based on tire slip state assessment. The computational procedure comprises the following steps:

Step 1: Calculate the lateral forces at interval intersection points: Determine the lateral forces at the boundaries of slip intervals using the tire slip ratio, vertical load, and road adhesion coefficient.

Step 2: Calculate the tire lateral forces: Compute the lateral forces of all four wheels according to Equation (45).

Step 3: Design the single-wheel control weight: Assign control weights to individual driving torques based on the deviation between each tire's lateral force and the slip-interval boundaries, which is given by

$$\eta_{4\mathrm{WD\_ij}} = \left(\tanh\left(\frac{F_y(\alpha) - F_y(\alpha_1)}{F_y(\alpha_2) - F_y(\alpha_1)}\right) + 1\right)\Big/2 \tag{49}$$

where α_1 is the intersection between the linear and nonlinear zones; α_2 is the intersection between the nonlinear and saturation zones.

Step 4: Calculate the torque control weight: The final torque control weight is determined as the minimum among the control weights of the four wheels, which is given by

$$\eta_{4\mathrm{WD1}} = \min(\eta_{4\mathrm{WD\_ij}}) \tag{50}$$

It is important to note that, according to the tire adhesion ellipse theory, a lower road adhesion coefficient reduces the total available tire force, thereby diminishing the potential additional yaw moment generated by longitudinal tire forces. To compensate for this limitation, the road adhesion coefficient is employed to constrain the distribution weights of both the steering angle and driving torque. The distribution weight of the driving torque is adjusted by

$$\eta_{4\mathrm{WD}} = \min(\eta_{4\mathrm{WD1}}, \mu) \tag{51}$$

Building on this foundation and accounting for the vehicle's steering characteristics, the control weights for the front- and rear-wheel steering angles are formulated as [9]

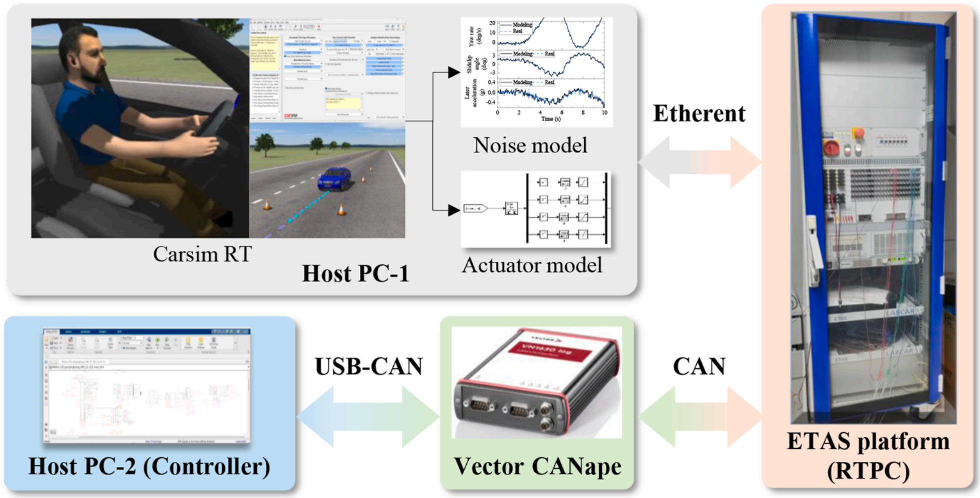

Fig. 8. The HIL platform.

Table 2
Parameters of the vehicle model.

Parameter	Value/unit	Parameter	Value/unit
m	1830 kg	b	1.65 m
a	1.4 m	B	1.6 m
h_g	0.53 m	k_f	−127800 N/rad
I_z	3234 kg·m^2	k_r	−109200 N/rad

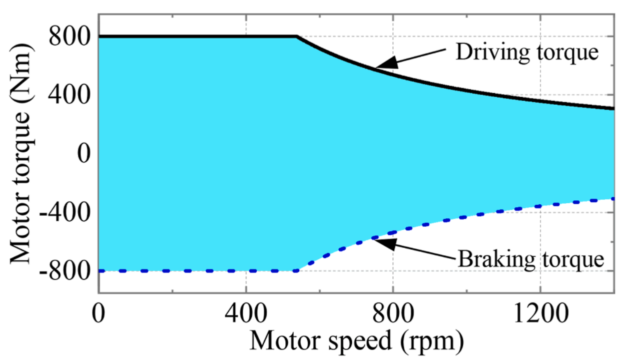

Fig. 9. The external characteristics of the in-wheel motor.

Table 3
Distribution characteristics of the measurement noise.

Signal	Mean	Variance
Sideslip angle (deg)	0	0.035
Yaw rate (deg/s)	0	0.37
Lateral acceleration (g)	0	0.022

Table 4
The controller parameters.

Controller strategy	MPC	Dyn	Proposed method
Controller parameter	$Q = \mathrm{diag}(200, 1800)$ $R = 0.12, N_p = 20, N_c = 15$ $\Delta M_{z\_max} = 5600, \Delta M_{z\_min} = -5600$		$c = 0.1,\ d = 1$ $\epsilon = 0.35,\ \lambda = 10$

$$\eta_{FWS} = (1 - \eta_{4WD})(\tanh(\omega_{re} * \delta_{sw}/2) + 1)/2 \tag{52}$$

$$\eta_{RWS} = 1 - \eta_{4WD} - \eta_{FWS} \tag{53}$$

Table 5
Assessment indicators of the control performance.

Performance indicator	Mathematical description
Path tracking error	$J_{epath} = \int_0^{t_n} [(f(t) - y(t))/E_{th}]^2 dt$
Heading error	$J_{\beta} = \int_0^{t_n} [v_x(t)\beta(t)/B_{th}]^2 dt$
Lateral stability	$J_{ay} = \int_0^{t_n} [a_y(t)/a_{y\_th}]^2 dt$
Driver workload	$J_{drive} = \int_0^{t_n} [\dot{\delta}_{sw}(t)/\dot{\delta}_{sw\_th}]^2 dt$
Yaw rate tracking error	$J_{ewr} = \int_0^{t_n} [(\omega_r(t) - \omega_{r\_ref}(t))/\omega_{r\_th}]^2 dt$

Table 6
Threshold values of the assessment indexes.

Threshold	E_{th}	B_{th}	$\dot{\delta}_{sw\_th}$	a_{y_th}	ω_{r_th}
Value	0.4	1.2	2	0.23	1

where η_{FWS} is the front-wheel steering angle control weight; η_{RWS} is the rear-wheel steering angle control weight.

3.3.4. Longitudinal force control

To ensure accurate tracking of the driver's desired speed, the target longitudinal acceleration is extracted directly from CarSim. Subsequently, the total required longitudinal force is computed by

$$F_x = m a_{x\_req} \tag{54}$$

where a_{x_req} is the driver's desired longitudinal acceleration.

3.3.5. Optimization of four-wheel driving torque distribution

In the lower-level torque distribution module, the total longitudinal force and additional yaw moment requested by the upper-level controller serve as the tracking targets. To mitigate wheel slip or spin, the slip ratios of the four wheels are incorporated into the cost function. Furthermore, the maximum motor torque and road adhesion limits are imposed as hard constraints to formulate the optimization problem for distributing longitudinal forces among four wheels. The resulting optimization formulation is given as

$$\begin{aligned} \min J &= \boldsymbol{W}_1(\boldsymbol{v} - \boldsymbol{B}_d\boldsymbol{u}_x) + \boldsymbol{W}_2\boldsymbol{u}_x \\ s.t. \quad & \frac{-T_{max}}{R_{tire}} \le F_{x\_ij} \le \frac{T_{max}}{R_{tire}} \\ & -\mu F_{z\_ij} \le F_{x\_ij} \le -\mu F_{z\_ij} \end{aligned} \tag{55}$$

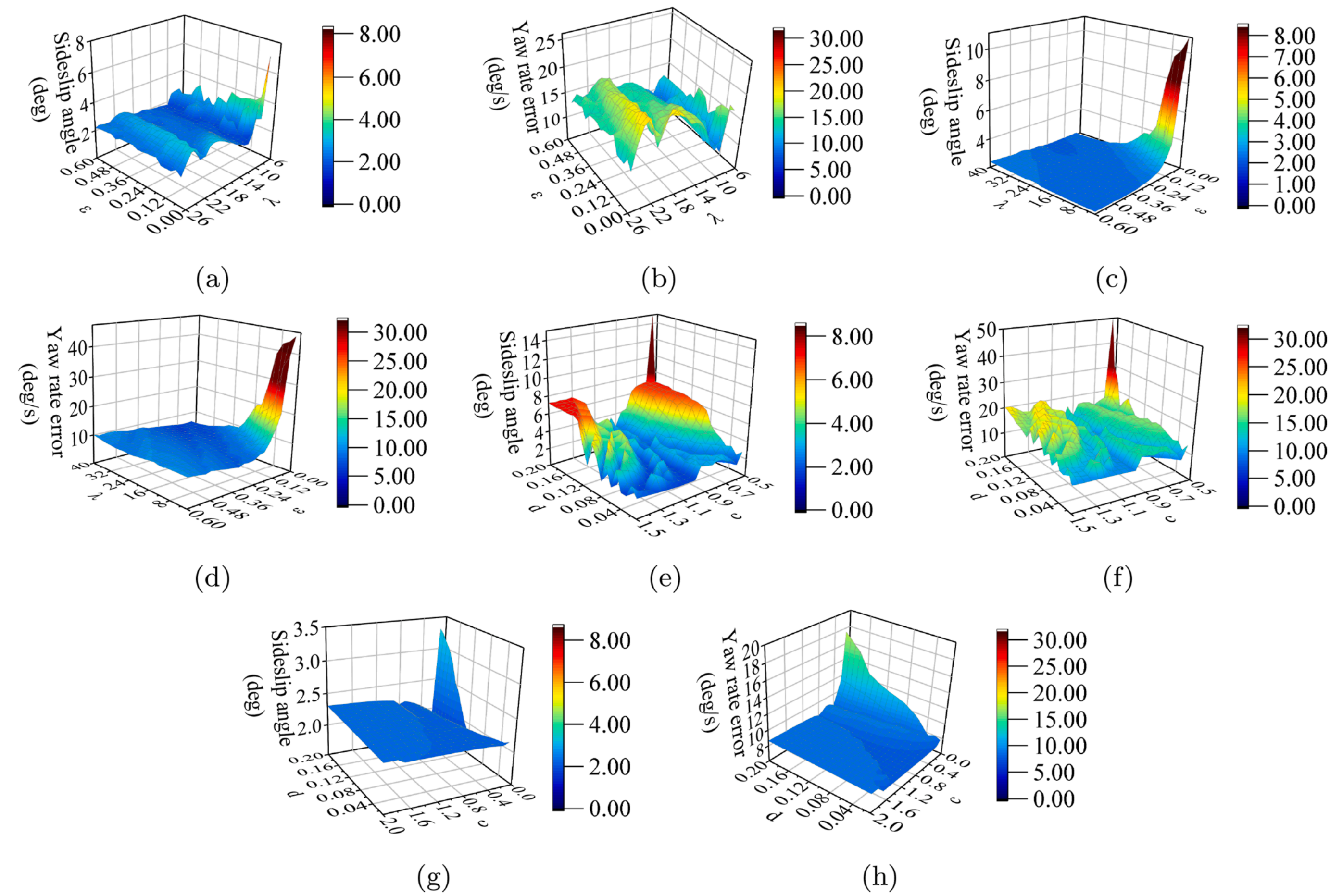

Fig. 10. The graph of vehicle performance variation with control parameter changes (a) sideslip angle with λ and ϵ (μ=0.35); (b) yaw rate error with λ and ϵ (μ=0.35); (c) sideslip angle with λ and ϵ (μ=0.85); (d) yaw rate error with λ and ϵ (μ=0.85); (e) sideslip angle with c and d (μ=0.35); (f) yaw rate error with c and d (μ=0.35); (g) sideslip angle with c and d (μ=0.85); (h) yaw rate error with c and d (μ=0.85).

where $\boldsymbol{v} = [F_x,\ \Delta M_{4\mathrm{WD}}]^T$ is the tracking target; $\boldsymbol{u}_x = [F_{\mathrm{xfl}},\ F_{\mathrm{xfr}},\ F_{\mathrm{xrl}},\ F_{\mathrm{xrr}}]^T$ is the longitudinal force at each wheel; $\boldsymbol{W}_1 = [0.001, 0.001]$ is the weighting coefficient vector for the tracking targets; $\boldsymbol{W}_2 = [W_{\mathrm{s}}, W_{\mathrm{s}}, W_{\mathrm{s}}, W_{\mathrm{s}}]$ is the weighting coefficient for the longitudinal tire force.

$$\mathbf{B}_{\mathrm{d}} = \begin{bmatrix} 1 & 1 & 1 & 1 \\ B_{\mathrm{d1}} & B_{\mathrm{d2}} & B_{\mathrm{d3}} & B_{\mathrm{d4}} \end{bmatrix} \tag{56}$$

$$\begin{aligned} B_{\mathrm{d1}} &= a\sin\delta_{\mathrm{f}} - 0.5l_{\mathrm{w}}\sin\delta_{\mathrm{f}} \\ B_{\mathrm{d2}} &= a\sin\delta_{\mathrm{f}} + 0.5l_{\mathrm{w}}\sin\delta_{\mathrm{f}} \\ B_{\mathrm{d3}} &= -b\sin\delta_{\mathrm{r}} - 0.5l_{\mathrm{w}}\sin\delta_{\mathrm{r}} \\ B_{\mathrm{d4}} &= -b\sin\delta_{\mathrm{r}} + 0.5l_{\mathrm{w}}\sin\delta_{\mathrm{r}} \end{aligned} \tag{57}$$

$$W_{\mathrm{s}} = \begin{cases} 0.004s_{\mathrm{tire}} + 0.0008 & \mathrm{abs}(s_{\mathrm{tire}}) \le 0.2 \\ 0.006s_{\mathrm{tire}} - 0.0002 & 0.2 < \mathrm{abs}(s_{\mathrm{tire}}) \le 0.5 \\ 0.02s_{\mathrm{tire}} - 0.0072 & \mathrm{abs}(s_{\mathrm{tire}}) > 0.5 \end{cases} \tag{58}$$

To facilitate code generation within Simulink, the active-set method is implemented to compute the required longitudinal tire forces. Subsequently, the driving torques for all four wheels are determined as

$$T_{\mathrm{ij}} = F_{x\_\mathrm{ij}} R_{\mathrm{tire}} \tag{59}$$

4. Hardware-in-the-loop verification

Comprehensive hardware-in-the-loop (HIL) tests were conducted to evaluate the performance of the proposed control strategy under various driving maneuvers. As illustrated in Fig. 8, the HIL test platform comprises two host PCs, a real-time personal computer (RTPC), and a CANape system. The primary host PC (PC-1) integrates a high-fidelity CarSim vehicle model with the LabCar environment to generate executable code, which is subsequently compiled and deployed to the RTPC. The RTPC simulates the vehicle dynamics and generates sensor signals. The secondary host PC (PC-2) serves as the controller, while the CANape system is utilized for CAN bus data acquisition and controller parameter calibration. The CAN bus operates at a bandwidth of 500 kbps. The vehicle model in the RTPC runs with a sampling frequency of 1 ms, whereas the communication cycle between PC-2 and the RTPC via the CAN bus is set to 10 ms.

The vehicle model employed in the HIL simulations is based on a standard CarSim template. Key vehicle parameters are summarized in Table 2. A first-order actuator dynamics model is integrated between the controller and the vehicle model to emulate real actuator behaviors. To reflect physical saturation limits, the front-wheel steering angle is constrained to [−30°, 30°], while the rear-wheel steering angle is limited to [−6°, 6°]. Based on the existing steer-by-wire system, the response time from command receipt to steady-state output is approximately 200 ms [36]. The steering angle response of the steer-by-wire system is modeled as

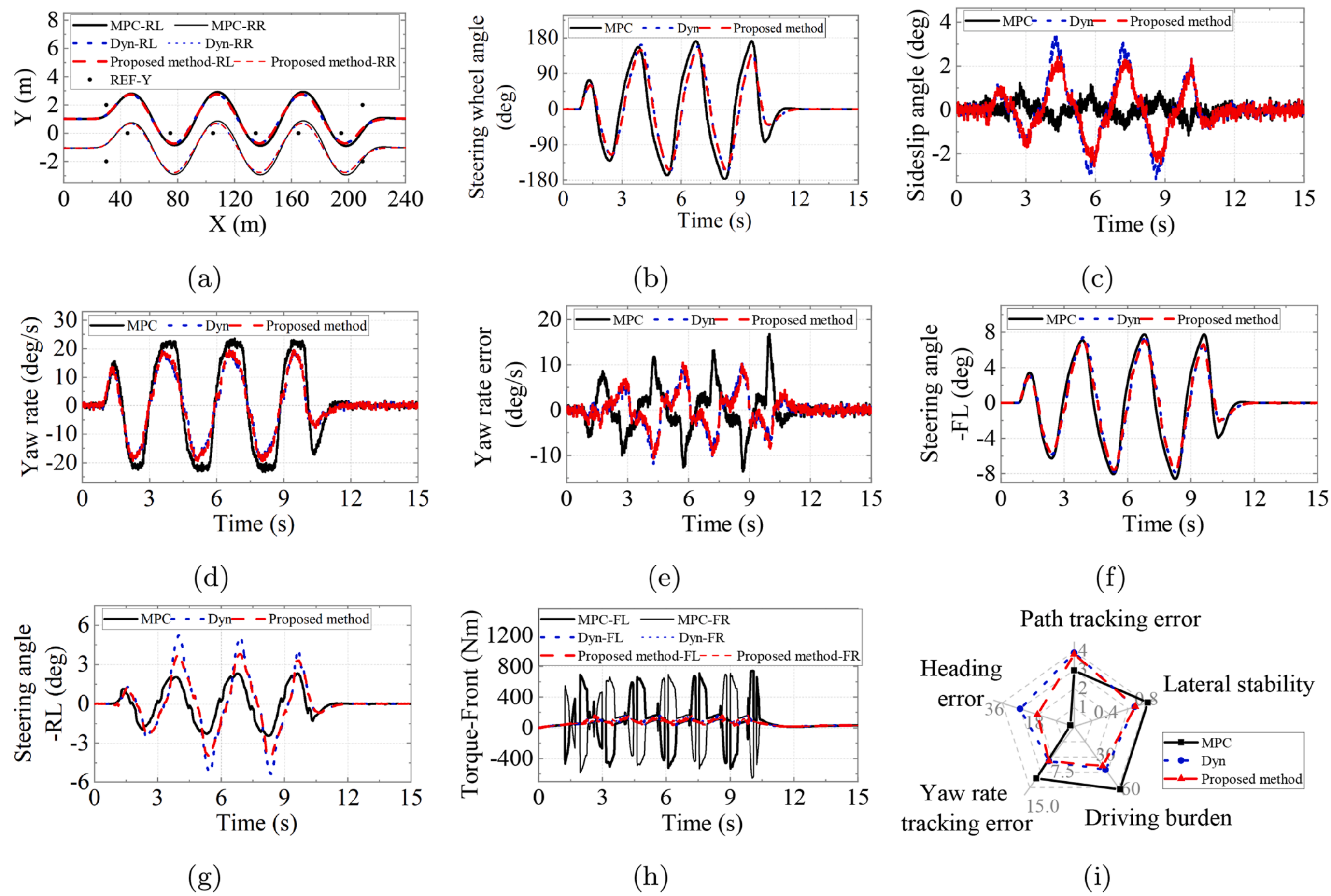

Fig. 11. The experimental results under the SLA maneuver: (a) rear wheel travel path; (b) steering wheel angle; (c) sideslip angle; (d) yaw rate; (e) yaw rate tracking error; (f) left-front wheel steering angle; (g) left-rear wheel steering angle; (h) front wheel driving torque; (i) the radar chart for comprehensive evaluation.

Table 7
The control performance under the SLA maneuver.

Control strategy		MPC	Dyn	Proposed method
Sideslip angle (deg)	MAX	1.23	3.43	2.55
	RMS	0.31	1.16	0.95
Yaw rate error (deg/s)	MAX	16.78	11.82	10.67
	RMS	4.34	3.54	3.54
Maximum yaw rate (deg/s)		23.52	19.67	19.85
Maximum lateral acceleration (g)		0.92	0.921	0.913
Maximum passing speed (km/h)		76	82	82

$$G_{\delta}(s) = \frac{\delta_{\mathrm{resp}}}{\delta_{\mathrm{req}}} = \frac{2209}{s^2 + 77.08s + 2209} \tag{60}$$

where δ_{resp} is the actual response angle of the wheel; δ_{req} is the steering angle signal received by the actuator.

Furthermore, the output torque of the in-wheel motor is constrained by its external torque-speed characteristics, as depicted in Fig. 9. To capture the dynamic response of the motor, it is modeled as a second-order system, whose transfer function is expressed as [37]

$$G_{\mathrm{Td}}(s) = \frac{T_{\mathrm{resp}}}{T_{\mathrm{req}}} = \frac{1}{0.0000125s^2 + 0.005s + 1} \tag{61}$$

where T_{resp} is the actual response torque of the motor; T_{req} is the torque signal received by the motor.

To emulate realistic vehicle state measurements, the zero-mean Gaussian white noise was superimposed on key state parameters, including the sideslip angle, yaw rate, and lateral acceleration. The statistical properties of the noises were derived by fitting empirical data acquired from in-vehicle sensors, as detailed in Table 3.

To comprehensively evaluate the performance of the proposed control framework, three representative test maneuvers are established: the slalom, the high-speed double-lane-change, and the low-adhesion double-lane-change. The proposed scheme is benchmarked against two comparative strategies: (i) a state-of-the-art control algorithm integrating model predictive control (MPC) and particle swarm optimization (PSO) [38], and (ii) a driver intention interpretation method based on a steady-state dynamics model (Dyn) [9]. This comparative setup specifically highlights the effectiveness of the proposed driver intention interpretation method. The controller parameters are summarized in Table 4, where $\boldsymbol{Q}$ denotes the state weighting matrix, $\boldsymbol{R}$ the control weighting matrix, N_p the prediction horizon, N_c the control horizon, and $\Delta M_{z\_\max}$ and $\Delta M_{z\_\min}$ the maximum and minimum allowable additional yaw moments.

To evaluate the overall performance of the proposed algorithm, five key metrics are adopted: path-tracking error, heading error, driver workload, lateral stability, and yaw-rate tracking error [39]. Path-tracking and heading errors quantify the trajectory-tracking performance, while the yaw-rate tracking error reflects the vehicle's ability to follow the driver intentions. The mathematical formulations of these evaluation indices are summarized in Tables 5 and 6 [9].

4.1. Parameter sensitivity analysis

To evaluate the sensitivity of the proposed control strategy to variations in controller parameters, simulations were performed under two representative driving scenarios: a high-adhesion double-lane-change

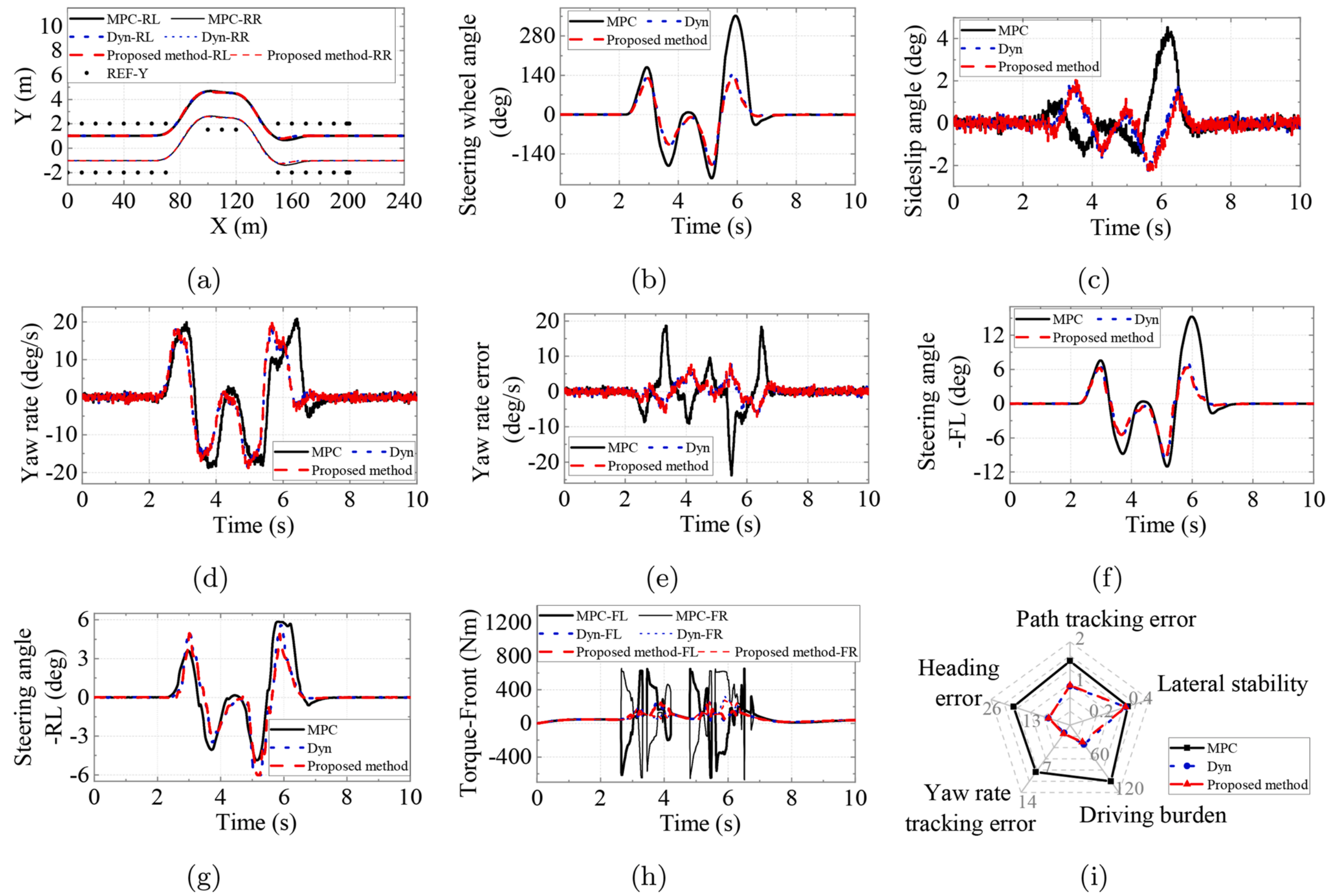

Fig. 12. The experimental results under the HDLC maneuver: (a) rear wheel travel path; (b) steering wheel angle; (c) sideslip angle; (d) yaw rate; (e) yaw rate tracking error; (f) left-front wheel steering angle; (g) left-rear wheel steering angle; (h) front-wheel driving torque; (i) the radar chart for comprehensive evaluation.

Table 8
The control performance under the HDLC maneuver.

Control strategy		MPC	Dyn	Proposed method
Sideslip angle (deg)	MAX	4.54	2.31	2.23
	RMS	1.05	0.64	0.64
Yaw rate error (deg/s)	MAX	23.82	7.63	8.45
	RMS	4.93	2.02	2.12
Maximum yaw rate (deg/s)		20.83	18.44	19.93
Maximum lateral acceleration (g)		0.941	0.997	1.01
Maximum passing speed (km/h)		92	116	120

Table 9
The control performance under the LDLC maneuver.

Control strategy		MPC	Dyn	Proposed method
Sideslip angle (deg)	MAX	29.45	7.07	1.73
	RMS	9.31	2.13	0.53
Yaw rate error (deg/s)	MAX	39.82	13.25	9.72
	RMS	12.02	3.75	1.62
Maximum yaw rate (deg/s)		44.66	14.83	15.61
Maximum lateral acceleration (g)		0.467	0.502	0.497
Maximum passing speed (km/h)		45	51	51

maneuver with v_x=90 km/h and μ=0.85, and a low-adhesion double-lane-change maneuver with v_x=50 km/h and μ=0.35.

In sliding mode control, the linear feedback gain λ directly determines the convergence rate toward the sliding surface. Larger values of λ yield faster convergence; however, excessively large gains may induce oscillations in system response. The switching gain ϵ primarily governs the disturbance rejection capability near the sliding surface. Although increasing ϵ enhances robustness and accelerates the switching process, overly high values can lead to excessive chattering. As shown in Fig. 10a-10b, under low-adhesion conditions, tire forces approach saturation, thereby limiting control redundancy. Consequently, even small variations in control parameters can trigger abrupt changes in vehicle behavior. Moreover, control performance exhibits greater sensitivity to changes in the linear feedback gain than to the switching gain. In contrast, Figs. 10c–d demonstrate that under high-adhesion conditions, the vehicle sideslip angle and yaw rate errors fluctuate only slightly within a certain range of λ and ϵ, indicating a broader optimal parameter region. This can be attributed to the higher force margin and parameter tolerance provided by tires on high-adhesion road surfaces. However, once the parameters exceed critical thresholds, the control accuracy deteriorates markedly, accompanied by sharp increases in both the sideslip angle and yaw rate errors.

Based on the sliding surface formulation, the weighting coefficients for the vehicle sideslip angle and yaw rate errors directly influence their contributions to the sliding mode dynamics. As illustrated in 10e-10h, the weighting coefficient for the yaw rate error has a more pronounced effect on vehicle motion, as the yaw rate error directly impacts the vehicle's ability to track the driver's commands. Furthermore, although the sensitivity to these parameters varies under high- and low-adhesion conditions, a suitable range exists to ensure satisfactory performance in both scenarios.

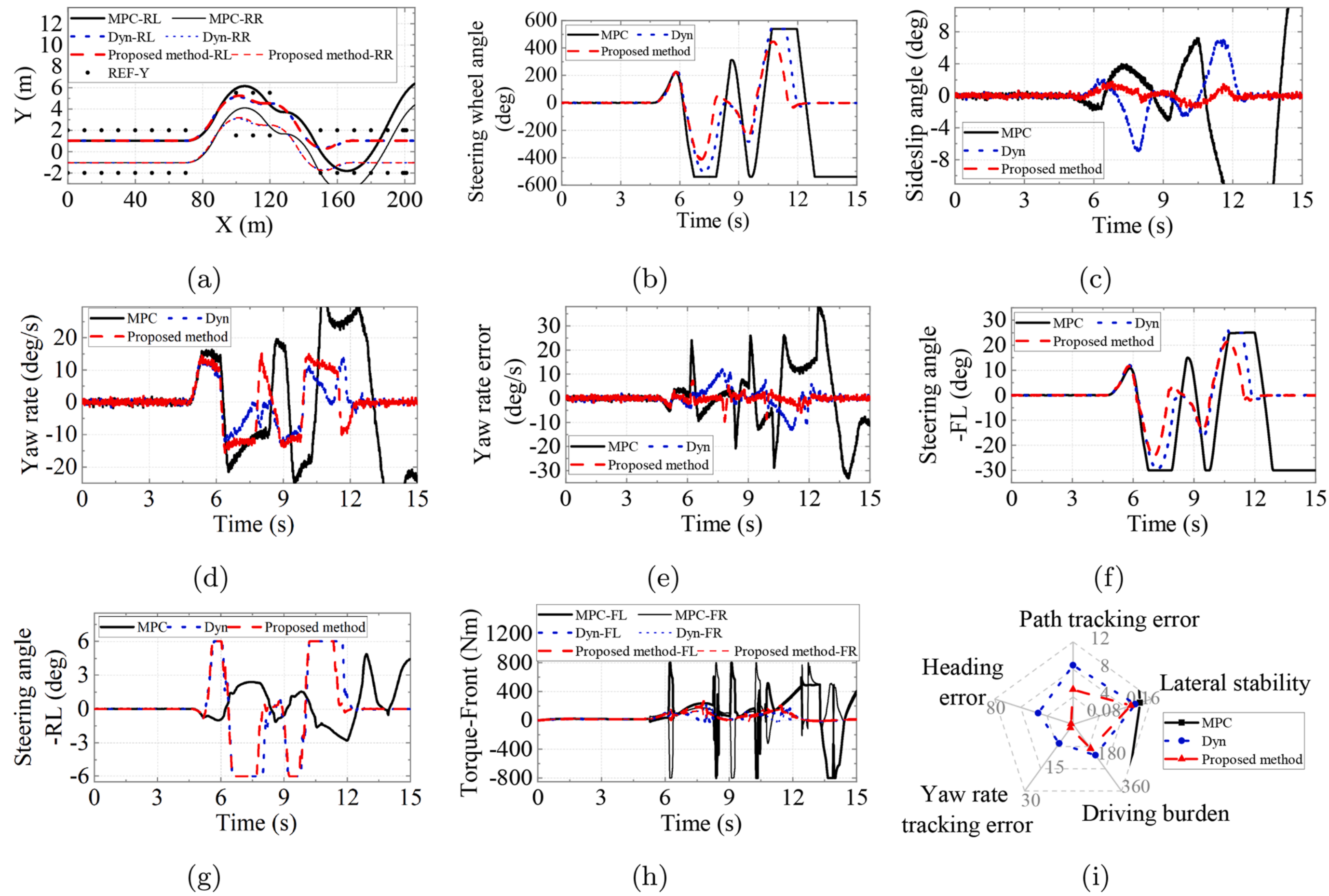

Fig. 13. The experimental results under the LDLC maneuver: (a) rear wheel travel path; (b) steering wheel angle; (c) sideslip angle; (d) yaw rate; (e) yaw rate tracking error; (f) left-front wheel steering angle; (g) left-rear wheel steering angle; (h) front wheel driving torque; (i) the radar chart for comprehensive evaluation.

4.2. Slalom maneuver

A slalom maneuver was conducted to evaluate the control performance of the proposed algorithm. The vehicle speed is maintained at 75 km/h, the driver preview time is 0.65 s, and the road adhesion coefficient μ is set to 0.85 [40]. The test results are presented in Fig. 11.

As demonstrated in Table 7, the proposed algorithm significantly outperforms the MPC control algorithm. Specifically, it reduces the yaw rate tracking error from 16.78°/s to 10.67°/s, thereby achieving better alignment with the driver's intentions. Additionally, the maximum yaw rate decreases from 23.52°/s to 19.85°/s, indicating improved yaw stability. The maximum passing speed also increases from 76 km/h to 82 km/h, reflecting enhanced vehicle maneuverability. Fig. 11f–h shows that the proposed algorithm primarily governs the steering control, with the front and rear wheel steering angles remaining similar. This indicates the activation of the oblique steering compensation module that leads to a larger vehicle sideslip angle. In contrast, the conventional MPC control algorithm primarily regulates four-wheel driving torques, resulting in a smaller sideslip angle but a larger yaw rate. Furthermore, Fig. 11a illustrates that the proposed algorithm achieves a smaller lateral offset of the rear wheels compared with the conventional MPC algorithm, demonstrating improved mobility. Finally, Fig. 11i highlights that the proposed algorithm, when combined with the kinematics-based driver intention interpretation method, outperforms the MPC control method in terms of driving workload reduction, driver intention tracking, and lateral stability maintenance.

4.3. High-speed double lane-change maneuver

A high-speed double lane-change maneuver was conducted to evaluate the effectiveness of the proposed algorithm under high-speed emergency obstacle avoidance scenarios. The vehicle speed is set to 90 km/h, the road adhesion coefficient μ is 0.85, and the driver preview time is 0.5 s. The simulation results are presented in Fig. 12.

As demonstrated in Table 8, the proposed algorithm significantly reduces the maximum yaw rate tracking error from 23.82°/s to 8.45°/s, indicating improved driver intention tracking capability. Additionally, the lateral acceleration increases from 0.941 g to 1.01 g, and the maximum passing speed rises from 92 km/h to 120 km/h, highlighting the algorithm's strong control performance in high-speed emergency obstacle avoidance scenarios. It is worth noting that both the proposed algorithm and the driver intention interpretation method based on the dynamic model exhibit superior control performance. As illustrated in Fig. Fig. 12a, when the vehicle travels approximately 150 m (at 6 s), the proposed algorithm rapidly adjusts the vehicle motion state and enables accurate tracking of the preview trajectory. This is achieved through the coordinated control of the front- and rear-wheel steering angles and four-wheel driving torques. In contrast, the MPC method fails to achieve coordinated steering control due to excessive steering wheel input from the driver. As a result, it relies solely on four-wheel driving torques, which significantly restricts vehicle maneuverability. Finally, as shown in Fig. 12i, the proposed algorithm outperforms the MPC control method in terms of driving intention tracking, lateral stability maintenance, preview trajectory tracking, and driving workload reduction. These

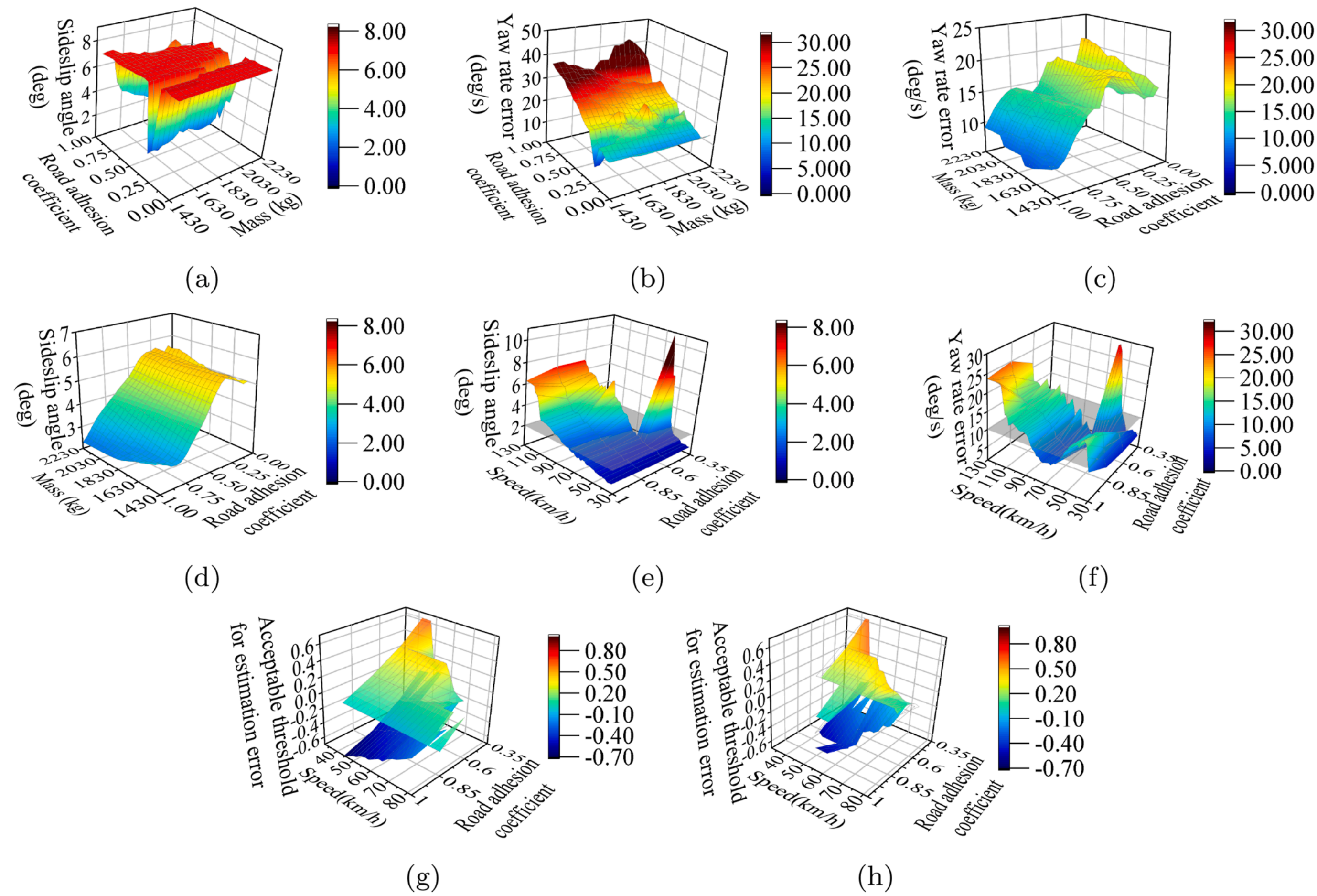

Fig. 14. The robustness analysis results: (a) maximum sideslip angle (μ=0.35); (b) maximum yaw rate error (μ=0.35); (c) maximum sideslip angle (μ=0.85); (d) maximum yaw rate error (μ=0.85); (e) maximum sideslip angle under different speeds; (f) maximum yaw rate error under different speeds; (g) acceptable road adhesion coefficient estimation error based on the sideslip angle threshold; (h) acceptable road adhesion coefficient estimation error based on the yaw rate error threshold.

results are consistent with those obtained using the dynamic model-based driver intention interpretation method (see Table 9).

4.4. Low-adhesion double lane-change maneuver

A low-adhesion double lane-change maneuver was also carried out to validate the control performance of the proposed algorithm under emergency obstacle avoidance scenarios with low road adhesion. The vehicle's travel path is depicted in Fig. 13a, with a speed of 50 km/h and a road adhesion coefficient of 0.35. The driver preview time is set to 0.5 s. The simulation results are shown in Fig. 13.

As illustrated in Fig. 13a, the vehicle under the MPC control strategy experiences severe tire slippage and fails to complete the maneuver. In contrast, the other two control strategies successfully complete the maneuver. According to Table 7, the proposed control strategy increases the maximum achievable passing speed from 45 km/h to 51 km/h, outperforming the MPC control strategy. Furthermore, compared with the dynamic interpretation method, the proposed driver intention interpretation method significantly reduces the sideslip angle from 7.07° to 1.73°, thereby substantially enhancing vehicle stability. As shown in Fig. 13d, at approximately 7 s, the dynamic driver interpretation mode rapidly reduces the vehicle yaw rate, whereas the proposed algorithm maintains the yaw rate near its maximum value. This improves vehicle stability and reduces steering wheel input. Finally, Fig. 13i demonstrates that the proposed algorithm outperforms the driver intention interpretation method based on the dynamic model in terms of preview trajectory tracking, driving workload reduction, and driving intention tracking.

4.5. Robust analysis

To evaluate the robustness of the proposed algorithm, simulations were conducted considering uncertainties in both vehicle mass and road adhesion. The vehicle mass was varied within the range of 1430–2230 kg, while the road adhesion coefficient ranged from 0.05 to 1. The test scenarios were consistent with those adopted in the sensitivity analysis.

As shown in Fig. 14, under high-adhesion conditions, when the estimated road adhesion coefficient is close to its actual value (i.e., with an estimation error within the range of [−0.05, 0.15]), the maximum sideslip angle and yaw rate errors remain relatively small (3° for the sideslip angle and 13°/s for the yaw rate), indicating strong robustness of the proposed algorithm. As the estimation error increases, both tracking errors increase significantly. In contrast, vehicle performance exhibits only minor fluctuations in response to variations in vehicle mass. These results demonstrate that the proposed algorithm is highly robust to mass uncertainty and can maintain robustness against road adhesion coefficient estimation error within a certain range. Furthermore, comparison between high- and low-adhesion scenarios indicates that the algorithm requires higher estimation accuracy of the road adhesion coefficient under low-adhesion conditions.

To further evaluate the robustness of the proposed control algorithm with respect to the accuracy of road adhesion estimation, a stability margin analysis was conducted over a range of vehicle speeds and road adhesion levels. The simulations considered vehicle speeds ranging from 30 km/h to 130 km/h. Performance thresholds were defined as 2° for the sideslip angle and 10°/s for the yaw rate error. To clearly illustrate the admissible range of estimation errors under acceptable performance conditions, the upper and lower bounds of the road adhesion coefficient estimation error are presented in a single figure.

As shown in Fig. 14e–h, vehicle speed has a significant impact on the tolerance to road adhesion coefficient estimation error. As vehicle speed increases, the admissible range of estimation error decreases markedly. At lower speeds, both the upper and lower bounds of the acceptable estimation error increase as the road adhesion coefficient decreases, resulting in a narrower allowable error range. Under high-speed maneuvers, this range shrinks sharply, further highlighting the increased sensitivity to estimation error under low-adhesion conditions. Overall, the proposed algorithm demonstrates strong robustness to road adhesion coefficient estimation error under low-speed, high-adhesion conditions; however, it requires higher estimation accuracy under high-speed, low-adhesion conditions.

5. Conclusion

This paper presents a global coordinated control framework for four-wheel steering and four-wheel drive systems based on tire slip state estimation. First, a hybrid feedforward control strategy comprising steady-state control, dynamic compensation, and oblique steering compensation is proposed to enhance vehicle mobility under normal driving conditions and stability under extreme conditions. Subsequently, a driver intention interpretation method that integrates conventional and oblique steering is introduced to alleviate driver workload. Simultaneously, a sliding mode control algorithm is employed to track the desired vehicle motion state. Furthermore, a coordination strategy for four-wheel steering angles and driving torques is developed based on tire slip state estimation. Finally, the proposed framework is validated through comprehensive driving scenarios using a hardware-in-the-loop test setup. Experimental results demonstrate that the proposed scheme increases the maximum achievable speed from 76 km/h to 82 km/h in the slalom maneuver and from 92 km/h to 120 km/h in the high-speed double-lane-change maneuver, thereby significantly enhancing handling performance.

CRediT authorship contribution statement

Xiaoxuan Yin: Writing – original draft, Investigation, Formal analysis, Data curation. **Lei Zhang:** Writing – review & editing, Supervision, Methodology, Funding acquisition, Conceptualization. **Xiaolin Ding:** Visualization, Validation, Software. **Fengchun Sun:** Supervision, Resources. **David Dorrell:** Writing – review & editing.

Declaration of competing interest

The authors declare the following financial interests/personal relationships which may be considered as potential competing interests: Lei Zhang reports article publishing charges was provided by Taishan Scholars Program. Lei Zhang reports statistical analysis was provided by National Natural Science Foundation of China. If there are other authors, they declare that they have no known competing financial interests or personal relationships that could have appeared to influence the work reported in this paper.

Acknowledgement

This work is partly supported by the Taishan Scholars Program under Grant No. tsqn202312310, partly supported by the National Natural Science Foundation of China under Grant No. 52272387 and No. 52394262, and partly supported by the China Postdoctoral Science Foundation under Grant No.2023M740244.

Data availability

Data will be made available on request.

References

[1] Alatawneh A, Ghunaim D. Towards vehicle electrification: a mathematical prediction of battery electric vehicle ownership growth, the case of Turkey. Green Energy Intell Transp 2024;3(4):100166. https://doi.org/10.1016/j.geits.2024.100166.

[2] He H, Sun F, Wang Z, et al. China's battery electric vehicles lead the world: achievements in technology system architecture and technological breakthroughs. Green Energy Intell Transp 2022;1(1):100020. https://doi.org/10.1016/j.geits.2022.100020.

[3] Pamidimukkala A, Kermanshachi S, Rosenberger JM, Hladik G. Barriers and motivators to the adoption of electric vehicles: a global review. Green Energy Intell Transp 2024;3(2):100153. https://doi.org/10.1016/j.geits.2024.100153.

[4] Wu J, Wang Z, Zhang L. Unbiased-estimation-based and computation-efficient adaptive MPC for four-wheel-independently-actuated electric vehicles. Mech Mach Theor 2020;154:104100. https://doi.org/10.1016/j.mechmachtheory.2020.104100.

[5] Wang Q, Zhao Y, Deng Y, Xu H, Deng H, Lin F. Optimal coordinated control of ARS and DYC for four-wheel steer and in-wheel motor driven electric vehicle with unknown tire model. IEEE Trans Veh Technol 2020;69(10):10809–19. https://doi.org/10.1109/TVT.2020.3012962.

[6] Liang Y, Li Y, Yu Y, Zheng L. Integrated lateral control for 4WID/4WIS vehicle in high-speed condition considering the magnitude of steering. Veh Syst Dyn 2020;58(11):1711–35. https://doi.org/10.1080/00423114.2019.1645343.

[7] Sun Y, Li R, Lu Z, Tian G. Design of four wheel steering and direct yaw moment control for unmanned vehicle with path tracking controller in extreme maneuvers. In: IEEE int. Conf. Unman. Syst. IEEE; 2021. p. 176–83. https://doi.org/10.1109/ICUS52573.2021.9641177.

[8] Abe Masato. Vehicle handling dynamics: theory and application. Singapore: Butterworth-Heinemann; 2015.

[9] Zhang L, Yin X, Wang Z, Sun F, Ding X. Hierarchical hybrid steering control for four-wheel-steering vehicles considering system delays. IEEE Trans Veh Technol 2024;74(2):2667–81. https://doi.org/10.1109/TVT.2024.3473305.

[10] Loyola J, Margolis D. Variable wheelbase reference for vehicle with active front and rear-wheel steering. Veh Syst Dyn 2022;60(8):2758–74. https://doi.org/10.1080/00423114.2021.1921814.

[11] Çakmak AT. 4 wheel steering system control unit design. Bal Can J Electr Comput Eng 2022;10(3):245–51. https://doi.org/10.17694/bajece.969569.

[12] Tan Q, Qiu C, Huang J, Yin Y, Zhang X, Liu H. Path tracking control strategy for off-road 4WS4WD vehicle based on robust model predictive control. Robot Autonom Syst 2022;158:104267. https://doi.org/10.1016/j.robot.2022.104267.

[13] Lin C, Siampis E, Velenis E. Path-tracking control at the limits of handling of a prototype over-actuated autonomous vehicle. Veh Syst Dyn 2024:1–23. https://doi.org/10.1080/00423114.2024.2361726.

[14] Cheng S, Peng HN, Yang C, Wang W, Li L. Chassis global dynamics optimization for automated vehicles: a multiactuator integrated control method. IEEE Trans Syst Man Cybern: Off Syst 2023;54(1):578–87. https://doi.org/10.1109/TSMC.2023.3311446.

[15] Yu Z, Luo R, Ma H, Hou Z. Yaw rate and roll motion control of 4IWMD/4WS vehicle based on active rear steering and torque coordination. IEEE, IEEE Intell Vehicles Symp 2024:1470–5. https://doi.org/10.1109/IV55156.2024.10588854.

[16] Li Y, Zhou W, Wang D. Stability coordinated control strategy of autonomous unmanned 4WID-4WIS vehicle based on APD-LQR and AFSMC. In: Proc. Inst. Mech. Eng., part D: J. Automob. Eng. SAGE Publications; 2024. p. 09544070241287250. https://doi.org/10.1177/09544070241287250.

[17] Niu R, Zhang W, Liu J, Chen G. Distributed vehicle longitudinal and lateral stability coordinated control for high-speed obstacle avoidance. In: Proc. CAA int. Conf. Veh. Control intell. IEEE; 2023. p. 1–6. https://doi.org/10.1109/CVCI59596.2023.10397196.

[18] Zhu S, Lu J, Zhu L, Chen H, Gao J, Xie W. Coordinated control of differential drive-assist steering and direct yaw moment control for distributed-drive electric vehicles. Electronics 2024;13(18):3711. https://doi.org/10.3390/electronics13183711.

[19] Liu H, Zhang L, Wang P, Chen H. A real-time NMPC strategy for electric vehicle stability improvement combining torque vectoring with rear-wheel steering. IEEE Trans Transp Electrif 2022;8(3):3825–35. https://doi.org/10.1109/TTE.2022.3153388.

[20] Qiao Y, Chen X, Yin D. Coordinated control for the trajectory tracking of four-wheel independent drive–four-wheel independent steering electric vehicles based on the extension dynamic stability domain. Actuators 2024;13(2):77. https://doi.org/10.3390/act13020077.

[21] Zhu S, Wei B, Liu D, Chen H, Huang X, Zheng Y, Wei W. A dynamics coordinated control system for 4WD-4WS electric vehicles. Electronics 2022;11(22):3731. https://doi.org/10.3390/electronics11223731.

[22] Teng F, Wang J, Jin L, Wang Z, Zhou Z, Liu Z. Cooperative control strategy of trajectory tracking and driving stability for distributed-drive vehicles under extreme conditions. Control Eng Pract 2024;147:105905. https://doi.org/10.1016/j.conengprac.2024.105905.
[23] Wang S, Zhang H, Zhao X, Zheng Z, Song H, Guo H. Research on lateral stability control strategy for distributed drive electric vehicles considering driving style. J Franklin Inst 2024;361(10):106921. https://doi.org/10.1016/j.jfranklin.2024.106921.
[24] Wang Z, Ding X, Zhang L. Chassis coordinated control for full x-by-wire four-wheel-independent-drive electric vehicles. IEEE Trans Veh Technol 2022;72(4):4394–410. https://doi.org/10.1109/TVT.2022.3222778.
[25] Zhang Z, Zheng L, Li Y, Li S, Liang Y. Cooperative strategy of trajectory tracking and stability control for 4WID autonomous vehicles under extreme conditions. IEEE Trans Veh Technol 2023;72(3):3105–18. https://doi.org/10.1109/TVT.2022.3216486.
[26] Wang G, Liu Y, Li S, Tian Y, Zhang N, Cui G. New integrated vehicle stability control of active front steering and electronic stability control considering tire force reserve capability. IEEE Trans Veh Technol 2021;70(3):2181–95. https://doi.org/10.1109/TVT.2021.3056560.
[27] Vignati M, Sabbioni E. A cooperative control strategy for yaw rate and sideslip angle control combining torque vectoring with rear wheel steering. Veh Syst Dyn 2022;60(5):1668–701. https://doi.org/10.1080/00423114.2020.1869273.
[28] Liang Jinhao, Lu Yanbo, Pi Dawei, Yin Guodong, Zhuang Weichao, Wang Faan, , et alLiang J, Lu Y, Pi D, Yin G, Zhuang W, Wang F. A decentralized cooperative control framework for active steering and active suspension: Multi-agent approach. IEEE Trans Transp Electrif 2021;8(1):1414–29. https://doi.org/10.1109/TTE.2021.3096992.
[29] Ding X, Wang Z, Zhang L, Liu J. A comprehensive vehicle stability assessment system based on enabling tire force estimation. IEEE Trans Veh Technol 2022;71(11):11571–88. https://doi.org/10.1109/TVT.2022.3193139.
[30] Rajamani Rajesh. Vehicle dynamics and control. US: Springer Science & Business Media; 2011.
[31] Xiao F, Hu J, Zhu P, Deng C. Chassis coordinated control based on ideal roll angle to improve vehicle stability. Veh Syst Dyn 2023;61(8):2074–102. https://doi.org/10.1080/00423114.2022.2101479.
[32] Yin D, Wang J, Du J, Chen G, Hu J. A new torque distribution control for four-wheel independent-drive electric vehicles. Actuators 2021;10(6):122. https://doi.org/10.3390/act10060122.
[33] Furuta K. Sliding mode control of a discrete system. Syst Control Lett 1990;14(2):145–52. https://doi.org/10.1016/0167-6911(90)90030-X.
[34] Rezaeian A, Zarringhalam R, Fallah S, Melek W, Khajepour A, Chen S, et al. Novel tire force estimation strategy for real-time implementation on vehicle applications. IEEE Trans Veh Technol 2014;64(6):2231–41. https://doi.org/10.1109/TVT.2014.2345695.
[35] Bakker E, Nyborg L, Pacejka HB. Tyre modelling for use in vehicle dynamics studies. SAE Trans 1987;96(2):190–204. https://www.jstor.org/stable/44470677.
[36] Xu S, Peng H, Tang Y. Preview path tracking control with delay compensation for autonomous vehicles. IEEE Trans Intell Transport Syst 2020;22(5):2979–89. https://doi.org/10.1109/TITS.2020.2978417.
[37] Zhou X. Research on obstacle avoidance control of hub motor intelligent vehicle. Wuhan: Wuhan University of Technology; 2021.
[38] Zhang H, Wang S, Zhao X, Zheng Z. Path tracking and handling stability coordinated control of 4WS and DYC for distributed in-wheel motor drive electric vehicle under extreme conditions. IEEE Trans Veh Technol 2024;73(12):18402–17. https://doi.org/10.1109/TVT.2024.3442303.
[39] Cao J. Studyon vehicle handling-stability evaluation approach based on human-vehicle-road closed-loop system. Shanghai Jiao Tong Univ. Shanghai: Ph.D. dissertation; 2015.
[40] Yu Z, Xia Q. Automobile theory. Beijing: China Machinery Press; 2009.